



**HAL**  
open science

## Osmium isotope evidence for rapid melt migration towards the Moho in the Oman ophiolite

Delphine Klaessens, Laurie Reisberg, David Jousselin, Marguerite Godard,  
Claire Aupart

### ► To cite this version:

Delphine Klaessens, Laurie Reisberg, David Jousselin, Marguerite Godard, Claire Aupart. Osmium isotope evidence for rapid melt migration towards the Moho in the Oman ophiolite. *Earth and Planetary Science Letters*, 2021, 572, pp.117111. 10.1016/j.epsl.2021.117111 . hal-03328806

**HAL Id: hal-03328806**

**<https://hal.univ-lorraine.fr/hal-03328806>**

Submitted on 30 Aug 2021

**HAL** is a multi-disciplinary open access archive for the deposit and dissemination of scientific research documents, whether they are published or not. The documents may come from teaching and research institutions in France or abroad, or from public or private research centers.

L'archive ouverte pluridisciplinaire **HAL**, est destinée au dépôt et à la diffusion de documents scientifiques de niveau recherche, publiés ou non, émanant des établissements d'enseignement et de recherche français ou étrangers, des laboratoires publics ou privés.



Distributed under a Creative Commons Attribution - NonCommercial - NoDerivatives 4.0  
International License

1 **Osmium isotope evidence for rapid melt migration towards the Moho in the**  
2 **Oman ophiolite**

3 Delphine KLAESSENS<sup>1\*</sup>, Laurie REISBERG<sup>1</sup>, David JOUSSELIN<sup>1</sup>, Marguerite GODARD<sup>2</sup>, Claire AUPART<sup>3</sup>

4 <sup>1</sup>Centre de Recherches Pétrographiques et Géochimiques, UMR 7358 CNRS - Université de Lorraine, 15  
5 rue Notre Dame des Pauvres, F-54501 Vandœuvre-lès-Nancy, France

6 <sup>2</sup>Géosciences Montpellier, CNRS, Université de Montpellier, Montpellier, France

7 <sup>3</sup>Physics of Geological Processes (PGP), The Njord Centre, Dept. of Geosciences, University of Oslo, PO  
8 Box 1048, N-0316, Oslo, Norway

9 (\*correspondence: [delphine.klaessens@univ-lorraine.fr](mailto:delphine.klaessens@univ-lorraine.fr))

10 **6499 words**

11        **Abstract**

12        The oceanic crust, covering two-thirds of the Earth’s surface, is formed along mid-oceanic ridges by  
13        crystallization at shallow levels of melts formed at depth by partial melting of mantle peridotite. Yet,  
14        the process of melt transport to the ridge axis remains poorly understood. Ophiolites, which provide a  
15        window into the uppermost mantle, contain dunite bodies often interpreted as relics of melt flow  
16        conduits, formed by pyroxene dissolution during melt-peridotite interaction. Here, we present  
17        structural and geochemical data on peridotites from the southeastern Oman ophiolite where three  
18        types of dunite, corresponding to the Moho transition zone (MTZ), the main and basal mantle  
19        sections, are identified. We focus on osmium isotopes, which are particularly well-adapted to tracing  
20        melt flow through peridotites. Osmium isotope signatures from host harzburgites accord with abyssal  
21        peridotite values and do not vary systematically with setting. In contrast, dunite Os compositions  
22        depend on structural context. Basal dunites display compositions similar to harzburgite values, while  
23        MTZ dunites have highly radiogenic compositions similar to those of the overlying crust, requiring  
24        extensive interaction with melts more radiogenic than MORB. Modeling shows that melts percolating  
25        through and equilibrating with dunite channels would acquire unradiogenic compositions, inconsistent  
26        with the observed Os signatures of MTZ dunites and lower crust. Thus, our findings require melt  
27        transport without equilibration with dunite or harzburgite, arguing for rapid or at least chemically  
28        isolated melt migration from the mantle source to the Moho.

29        ***233 words***

30 **Keywords**

31 Oman ophiolite, Mantle, Osmium isotopes, Melt migration, Dunite

32 **Highlights**

- 33 1. Distinction of three types of dunite in the mantle section of SE Oman ophiolite
- 34 2. Strong correlation between dunite Os isotope composition and structural context
- 35 3. MTZ dunites interacted extensively with melts more radiogenic than MORB
- 36 4. High  $^{187}\text{Os}/^{188}\text{Os}$  at odds with melt transport by percolation in dunite channels
- 37 5. Rapid/chemically isolated melt transport needed to maintain radiogenic signatures

## 38 **1. Introduction**

39 Melt migration processes beneath mid-oceanic ridges remain controversial, engendering a diversity of  
40 models based on structural (Nicolas, 1986), geochemical (Kelemen et al., 1995), petrological (Morgan  
41 and Liang, 2003) and numerical studies (Ahern and Turcotte, 1979; Stevenson, 1989). One strong  
42 constraint is the existence of disequilibrium between shallow mantle peridotites and mid-ocean ridge  
43 basalts (MORBs) (O'Hara, 1965; Stolper, 1980), manifested notably by undersaturation of  
44 orthopyroxene (opx) in MORBs. Melt-peridotite interactions can result in pyroxene dissolution in the  
45 host peridotite (Kelemen, 1990; Lambart et al., 2009; Morgan and Liang, 2003), forming dunite if  
46 continued to completion. The origin of ophiolitic dunite bodies is commonly attributed to this process  
47 (Boudier and Nicolas, 1977, 1995; Büchl et al., 2002, 2004; O'Driscoll et al., 2012), which may generate  
48 dunite channels providing transport pathways for ascending melts (Kelemen et al., 1995). In such  
49 channels, melts are isolated from equilibration with the surrounding peridotite, but may equilibrate  
50 with the dunite.

51 The Oman ophiolite is well-suited for the study of melt migration beneath mid-oceanic ridges. This  
52 large (>20 000 km<sup>2</sup>), well-exposed segment of oceanic lithosphere, formed ~95 Ma ago along a rapid  
53 spreading center (Boudier et al., 1997; Nicolas et al., 2000a; Rioux et al., 2012), provides a window  
54 into the uppermost mantle, which outcrops over >50% of its surface. The Re-Os radiometric system, in  
55 which <sup>187</sup>Re decays to <sup>187</sup>Os ( $t_{1/2} = 41.6$  Ga,  $\lambda = 1.666 \times 10^{-11}$ ) (Smoliar et al., 1996), is a particularly useful  
56 tool for studying mantle melt transport. The contrasting behavior of these two elements during partial  
57 melting (rhenium is moderately incompatible while osmium is compatible) creates Earth reservoirs  
58 with strikingly different Re/Os ratios, producing over time contrasting Os isotope ratios. Recycled  
59 oceanic crust and sediments develop highly radiogenic Os compositions while mantle peridotites  
60 remain unradiogenic. When melt migrates through dunite, the isotopic and elemental compositions of  
61 incompatible elements (e.g. light rare earth elements) are rapidly overprinted in the dunite by  
62 equilibration with the magma, which has much higher concentrations of these elements. For Os, the  
63 mass balance is reversed, allowing gradual changes in Os isotope composition to be recorded in the  
64 dunite as melt progressively passes through.

65 Here, we present structural observations and geochemical data on melt migration and dunite  
66 formation from peridotites from the southeastern Oman ophiolite. We focus on Os isotopes, tracers  
67 exceptionally well-adapted to studying melt-peridotite interactions. Implications of our results for  
68 melt transport mechanisms are modeled in light of the structural context of each sample.

## 69 **2. The Oman ophiolite**

### 70 **2.1. *Internal structure***

71 As documented by early studies (e.g. Boudier and Coleman (1981); Lippard et al. (1986); Nicolas et al.  
72 (2000a)), the Oman ophiolite consists of a >15 kilometer thick dominantly harzburgitic mantle section,  
73 overlain by a complete mafic crust. Our study focuses on the mantle section. This domain was first  
74 detailed by Boudier and Coleman (1981), based on a cross-section in the Wadi Tayin massif. The  
75 uppermost few hundred meters beneath the crust correspond to the Moho Transition Zone (MTZ), a  
76 primarily dunitic layer of variable thickness. The MTZ has been extensively studied (e. g. Boudier and  
77 Nicolas (1995); Godard et al. (2000); Koga et al. (2001); Rospabé et al. (2018)) and is interpreted as a  
78 melt storage and reaction zone, where ascending melts stagnate beneath the crust-mantle interface  
79 (Moho). These melts dissolve orthopyroxene of the host harzburgite, producing both pure dunite and  
80 "melt-impregnated" dunite with interstitial plagioclase, pyroxene and occasional amphibole, as well as  
81 rare cumulate gabbro lenses (<5%). In the lowermost MTZ, interfingering relationships between  
82 harzburgite and dunite with orthopyroxene relics suggest a melt-peridotite reactional origin for the  
83 dunite (Nicolas and Prinzhofer, 1983). Furthermore, the olivine Mg# [=  $Mg/(Mg+Fe_{total})_{at}$ ] is similar in  
84 the MTZ and underlying harzburgite, whereas spinel TiO<sub>2</sub> content in the MTZ is higher, indicating  
85 dunite arose from equilibration with TiO<sub>2</sub>-rich primary melts rather than crystal fractionation (Koga et  
86 al., 2001).

87 Beneath the MTZ, the primarily harzburgitic main mantle section (MMS) comprises most of the  
88 ophiolite volume. The exact distribution of dunite within the MMS is unclear and its estimated  
89 proportion varies between studies (e. g. <5% for Boudier and Coleman (1981) and 5-15% for Lippard et

90 al. (1986)). Dunite occurs either as planar and irregular bodies with dimensions up to ~20 meters  
91 (Bartholomew, 1983), crosscutting the mantle fabric, or more rarely, as thin concordant bands.  
92 Crosscutting gabbro and pyroxenite dikes are occasionally observed.

93 At the bottom of the mantle section near the basal thrust, a highly deformed, basal banded unit (BBU)  
94 is often observed. In this section, Boudier and Coleman (1981) report subequal proportions of  
95 harzburgite (or occasionally lherzolite) and concordant dunite bands, varying in thickness from 0.1 to  
96 several meters. Lippard et al. (1986) also note significantly increased dunite abundance near the base.  
97 These basal dunites have never been thoroughly nor systematically studied.

98 Braun and Kelemen (2002) determined a power law relationship between dunite width and  
99 cumulative abundance, which they used to support a model of melt transport to the ridge in  
100 coalescing dunite channels. The mid to large-sized dunites in their study were measured in the Muscat  
101 massif (Fig. 1). The proximity with the basal thrust and the exceptionally high dunite abundance (18-  
102 46%) of this small massif suggest that it is derived from the BBU.

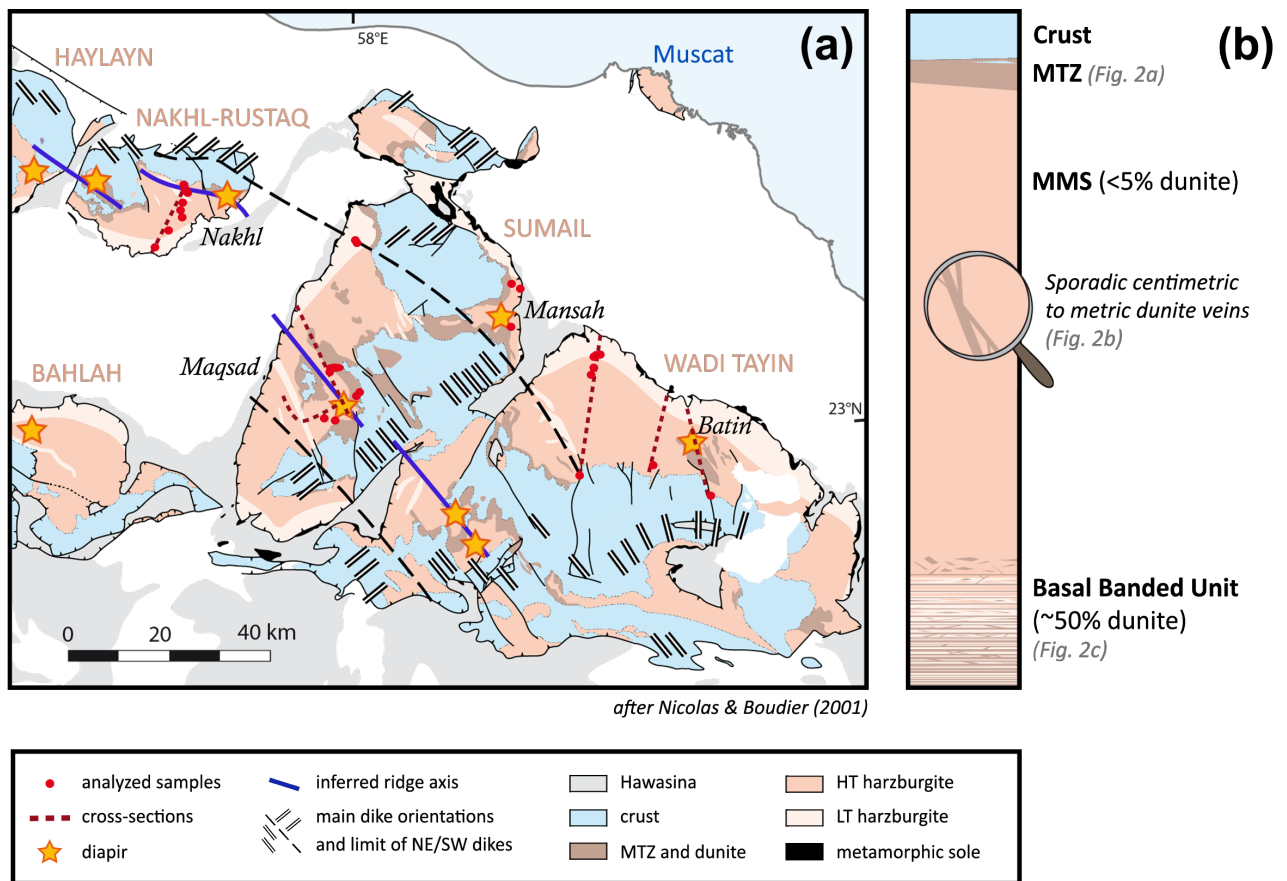
## 103 **2.2. Geodynamic context**

104 The geodynamic context of the Oman ophiolite has long been controversial. The ophiolite presents  
105 several characteristics akin to those of fast spreading ridges (e. g. magma chamber shape, mantle  
106 structure, crustal continuity, structure and thickness variation...) (Boudier et al., 1997; Nicolas et al.,  
107 2000a). Moreover, basalts above the sheeted dike complex (V1, Geotimes unit) display MORB-like  
108 compositions (Ernewein et al., 1988; Godard et al., 2006). However, upper lavas (V2, Lasail unit, found  
109 in northern Oman) overlying hydrothermal deposits display island arc affinities (Alabaster et al., 1982;  
110 Ernewein et al., 1988), suggesting ophiolite formation in a supra-subduction setting. As these upper  
111 units clearly postdate most of the crustal accretion, and probably the recorded mantle flow, this origin  
112 has been disputed. However, reappraisal of the Geotimes unit (MacLeod et al., 2013) and dating of the  
113 metamorphic sole (Guilmette et al., 2018) strongly argue for accretion of the entire ophiolite from a  
114 hydrated mantle above a subducting slab. Nevertheless, the critical parameters controlling magmatic  
115 accretion at the ridge are spreading rate and presence or absence of a magma chamber, regardless of

116 the broader tectonic context. Thus, the Oman ophiolite remains a well-suited laboratory for studying  
117 melt migration in the mantle beneath accretion centers, as long as we focus on features  
118 contemporaneous with the asthenospheric mantle flow.

119 Systematic petrostructural mapping (Nicolas et al. (2000a) and references therein) revealed the  
120 deformation temperatures of the peridotite and their spatial variation. Coarse-grained granular and  
121 porphyroclastic textures with well-recovered sub-structures are ascribed to asthenospheric  
122 deformation at the spreading center. Finer-grained porphyroclastic textures with varying degrees of  
123 recrystallization into neoblasts, mostly restricted to the borders of the massifs, reflect overprinting  
124 low-temperature deformation, associated with ophiolite emplacement. Later faulting is limited. Thus,  
125 the ophiolite can be seen as a fossilized piece of oceanic lithosphere, dissected by erosion and slightly  
126 tilted following the dip of the Moho.

127 In the southeastern part of the ophiolite, the focus of our study, a NW-SE paleo-spreading center was  
128 identified from dike orientations, which trend NW-SE in the center of the Sumail massif and  
129 perpendicularly (NE-SW) to the north and south of this central zone (Fig. 1) (Boudier et al., 1997). The  
130 position of this spreading center is inferred from the alignment of several harzburgitic mantle diapirs,  
131 defined by steeply plunging lineations with radial horizontal lineations at their outskirts (Jousselin et  
132 al., 1998). Solid-state flow lineations in the harzburgite and MTZ, and magmatic lineations in the  
133 overlying crust are remarkably parallel, indicating that the mantle lineations formed before the gabbro  
134 was frozen. These observations show that harzburgite diapirs, MTZ formation and ridge accretion  
135 were contemporaneous, with diapirs being likely feeding centers for the overlying ridge segments.



136

137 **Fig. 1.** Sample locations and structure of the southeastern part of the Oman ophiolite. (a) Simplified  
 138 geological map of the southeastern massifs (Nakhl-Rustaq, Sumail, Wadi Tayin and Haylayn) of the  
 139 Oman ophiolite (after Nicolas and Boudier (2001)) showing the sample locations (red dots) and the  
 140 spatial distribution of the crust, Moho Transition Zone (MTZ), mantle and metamorphic sole sections.  
 141 Most samples were collected along cross-sections (bold burgundy dotted lines) in on-axis and off-axis  
 142 settings. Hawasina sediments, inferred ridge axis (bold blue lines), mantle diapirs (stars), main dike  
 143 orientations (double black lines) and limits of NE-SW dikes (black dashed curves) are also shown. Batin  
 144 dunite (in dark brown) is visible in the Batin area in the eastern part of the Wadi Tayin massif, below  
 145 the diapir. (b) Schematic mantle cross-section based on field observations, showing the distribution of  
 146 the three types of dunite described in the text: Mantle transition zone (MTZ), sporadic centimetric to  
 147 metric veins in the main mantle section (MMS) and abundant bands in the basal banded unit (BBU).  
 148 (For interpretation of the colors in the figure(s), the reader is referred to the web version of this article.)

149

### **2.3. Definition of three types of dunite in the mantle section**

150

To clarify dunite distribution, we made observations and collected samples along six cross-sections

151

traversing the mantle section, in diapiric and non-diapiric areas in the Nakhl-Rustaq, Sumail (Maqsad

152

diapir) and Wadi Tayin massifs (Fig. 1 and Fig. A.1). Complementary observations were made at sites

153

near Muscat, at the base of the Haylayn massif and in the Batin area in the eastern part of Wadi Tayin.

154

Our observations distinguish three types of dunite, each associated with a specific part of the mantle

155

section (Fig. 1-2; dunite thicknesses in Table A.1):

156

(1) Moho Transition Zone (MTZ) (Fig. 2a): As noted by previous studies (Boudier and Nicolas, 1995;

157

Koga et al., 2001; Rospabé et al., 2018), the MTZ is composed of pure and plagioclase/clinopyroxene-

158

impregnated dunites, and reaches thicknesses of 50-500 meters above harzburgite diapirs, and usually

159

<30 meters far from diapirs. Dunitic lenses several meters wide, interlayered with harzburgite, are

160

sometimes found in the hundred meters underlying the MTZ. The MTZ volume is so large that it can

161

be represented on maps including several massifs (scales of 1/1 000 000 to 1/500 000) (Fig. 1).

162

(2) Harzburgitic main mantle section (MMS): Discordant gabbroic and pyroxenitic dikes rimmed by

163

dunitic reaction zones crosscut sporadically the MMS harzburgite (Fig. 2b left), as described by

164

Boudier and Coleman (1981). In some cases, all of the melt was extracted from the dike, leaving only

165

the dunitic reaction zones, several centimeters to 5 meters wide, crosscutting the mantle fabric

166

(henceforth such features referred to as “dunite veins”) (Nicolas et al. (2000b) and references

167

therein). Angular contacts, harzburgite blocks trapped between dunite veins, and stockwork-like

168

geometry suggest a hydrofracturing origin for the magmatic dikes from which the dunitic reaction

169

zones formed (Fig. 2b right). The crosscutting nature of these veins indicates they post-date

170

asthenospheric flow, but several examples of partially tectonically transposed dunite veins suggest

171

they also could form in the flowing mantle. Centimetric dunites parallel to the foliation are also

172

observed in the MMS (henceforth “dunite bands”) (insert in Fig. 2b), possibly representing extreme

173

examples of transposed veins. All the MMS dunites, even those in harzburgite diapirs, represent a

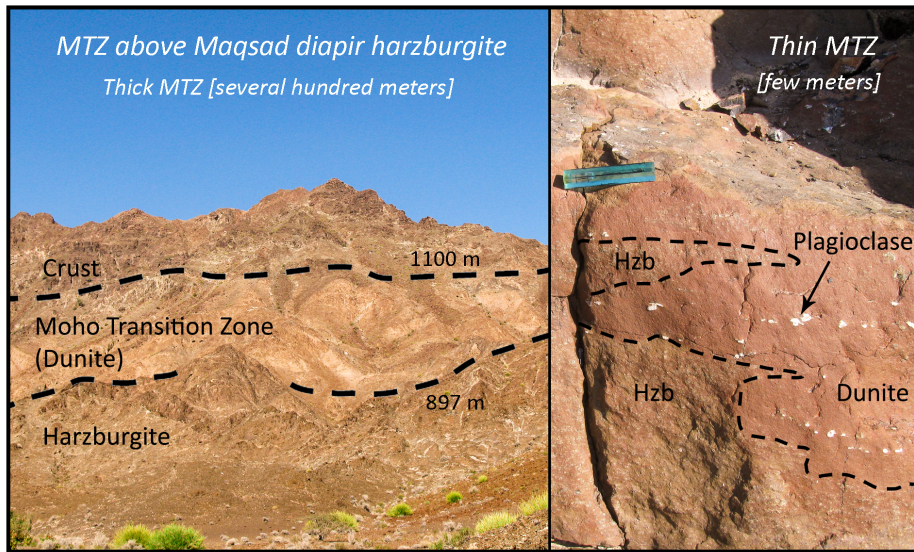
174

negligible, unmappable fraction of the mantle volume.

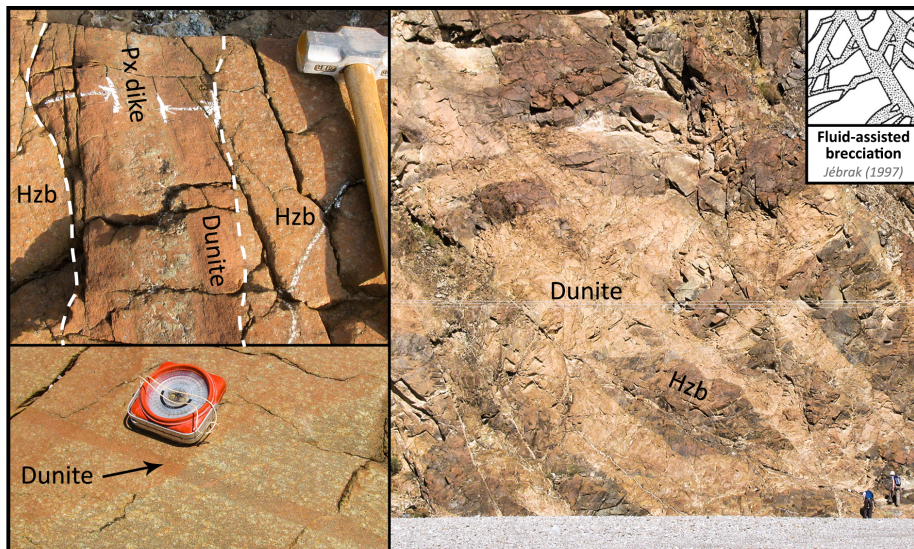
175 (3) Basal banded unit (BBU): This zone often hosts abundant, mainly concordant dunitic bands (Fig.  
176 2c). These are usually centimeters to meters thick, rarely up to 20 meters, with the largest being  
177 mappable locally at the 1/10 000 scale. They are sometimes composed of opx-poor harzburgite  
178 instead of dunite. Coarse-grained samples sometimes occur between fine-grained ones (Table A.2)  
179 and at the top of the unit, suggesting that the transition from the low-temperature to the high-  
180 temperature domain is irregular, and that the BBU is thicker than the low-temperature domain. In the  
181 Wadi Tayin and Nakhl-Rustaq massifs, the top of this unit, where coarse-grained asthenospheric  
182 deformation is preserved, includes 3-20 meter "blobs" of dunite, often with several dunite veins  
183 branching into them, exactly as drawn by Bartholomew (1983). Such blobs are rare in the MMS (none  
184 in our cross-sections). The concentration of dunitic bands in the BBU is poorly understood. Lippard et  
185 al. (1986) suggested that ophiolite thrust-related extreme deformation of scattered dunite bodies in  
186 the mantle section could explain the basal dunite banding; however, this would not explain the higher  
187 dunite content in this section relative to the MMS, and the fact that parts of the banding, as well as  
188 the dunitic blobs, display asthenospheric deformation textures.

189 An exceptional fourth type of dunite is exposed in the Batin area, consisting of a dunite body >9  
190 kilometers long, 2 kilometers wide and several hundred meters thick (Fig. 1), evident on the USGS  
191 Wadi Tayin geological map and clearly visible in the field and on aerial photographs. This body was  
192 sampled by the ICDP Oman Drilling Project and several dedicated studies, including our own, are  
193 ongoing. Apart from the Batin area, no dunite larger than 30 meters, or similar to those at the base of  
194 the ophiolite, was found in the MMS. This is true even in the diapiric areas, thought to represent  
195 feeding zones for the overlying crust.

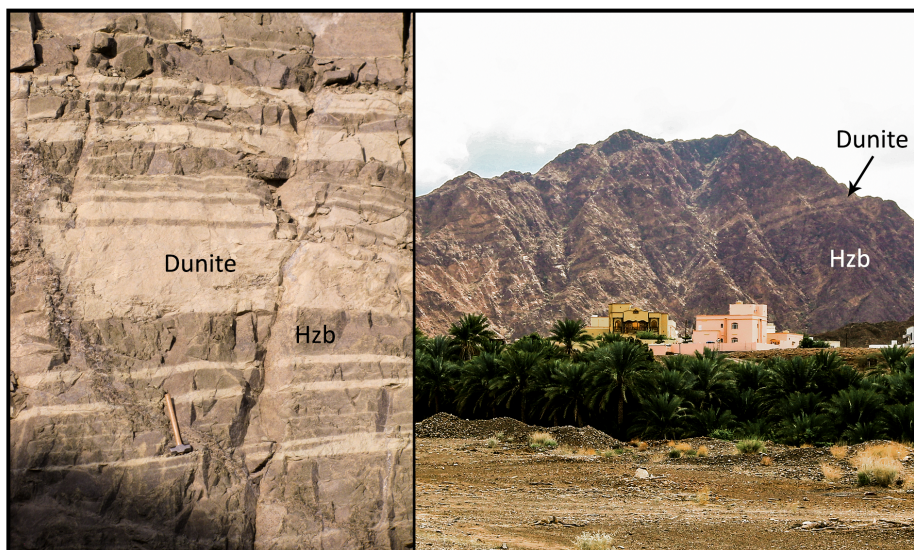
**(a) Moho Transition zone (MTZ) at the summit of the mantle section**



**(b) Sporadic dykes in the main mantle section**



**(c) Abundant concordant dunite bands at the base of the ophiolite**



197 **Fig. 2.** Field photographs illustrating the three types of dunite observed in the mantle section of the SE  
198 Oman ophiolite. **(a)** Moho Transition Zone (MTZ): Left, landscape-view of the thick dunitic MTZ just  
199 beneath the crust in the Maqсад diapir region; Right, plagioclase-impregnated dunite of the thin MTZ  
200 from the Nakhl-Rustaq massif in contact with residual harzburgite. **(b)** Sporadic veins in the main  
201 mantle section (MMS) of the Nakhl-Rustaq massif: Left, thin pyroxenite dike with dunite reaction zone;  
202 insert, concordant dunite band. Right, cross-cutting plurimetric dunite veins (16OD1) to compare with  
203 insert showing sketch of a breccia hydrofracture network from Jébrak (1997). **(c)** Abundant concordant  
204 dunitic bands at the base of the ophiolite: Left, succession of dunitic and harzburgitic bands in the  
205 basal section from the northern Sumail massif; Right, landscape-view of the basal banded unit in the  
206 Wadi Tayin massif. Hzb, harzburgite.

207 **3. Samples and analytical techniques**

208 Samples were selected from the three types of dunite (19 from 81 collected dunites, chosen for  
209 freshness and variety) and host harzburgite (20 from 140 collected harzburgites) in the mantle  
210 sections of the Nakhl-Rustaq, Sumail, Wadi Tayin and Haylayn massifs ([Fig. 1](#); UTM coordinates in  
211 [Tables A.2-3](#)). In six cases, dunite and harzburgite were collected in close proximity (<1 meter) ([Table](#)  
212 [A.1](#)). Sampling localities include both off-axis (e.g. Nakhl-Rustaq and Wadi Tayin massifs, Mansah  
213 diapir in Sumail massif) and on-axis (e.g. Maqsad diapir in Sumail massif) settings.

214 Dunite structural data and petrographic descriptions of all analyzed samples are given in [Tables A.1-2](#)  
215 (complementary descriptions of non-analyzed samples in [Table A.9](#)). Harzburgites are moderately to  
216 highly serpentinized and have coarse-grained porphyroclastic textures, except for four fine-grained  
217 samples from the BBU. Dunites are moderately to highly serpentinized, with higher degrees of  
218 serpentinization in the MTZ and the BBU. Sulfides are very rare and small in both lithologies. Medium  
219 to high-temperature porphyroclastic and granular textures are observed among all three types of  
220 dunite. Grain size, spinel abundance, crystal shape and serpentinization degree do not vary  
221 systematically, making it difficult to distinguish different dunite types simply from examination of hand  
222 specimens or thin sections. Nevertheless, basal dunites (1) never contain plagioclase, and (2) often  
223 contain orthopyroxene relics. Our dunitic samples include seven pure dunites (98.0-99.5%<sub>OI</sub> and <0.5-  
224 2.0%<sub>SpI</sub>), eight containing pyroxene relics (<1.5%<sub>Px</sub>), three impregnated with plagioclase and/or  
225 pyroxene, and one olivine troctolite.

226 Whole-rock major and trace element compositions ([Tables A.3-5](#)) were determined respectively by the  
227 SARM at CRPG using an ICP-OES iCap6500 and at Géosciences Montpellier (AETE-ISO University of  
228 Montpellier, France) using an Agilent 7700X quadrupole ICP-MS. After chemical separation, Os isotopic  
229 analyses ([Tables A.6-8](#)) were done at CRPG by NTIMS using a Finnigan MAT262 mass spectrometer.  
230 Details of analytical methods are provided in the [Supplementary Material](#).

#### 4. Variations in major element and Os isotope compositions with structural context

Harzburgites from both the main and basal sections have Mg# mostly from 0.900 to 0.916 and Os concentrations from 2.27 to 6.29 ppb (Fig. 3b, 4a; Table 1 and Tables A.3, 6-7). Basal harzburgites generally have lower Al<sub>2</sub>O<sub>3</sub> (0.39-0.63 wt.%) than MMS harzburgites (0.48-0.96 wt.%), except for two samples (16OL27B and 16OL29), whose compositions (0.92 and 1.21 wt.%) approach those of clinopyroxene-bearing harzburgites from Godard et al. (2000) (Fig. 3a). Plagioclase-impregnated, orthopyroxene-poor harzburgite 16OD5C from the uppermost MMS displays the highest FeO (8.76 wt.%) and lowest Os content of all of the harzburgites (Fig. 3b, 4a). Values of <sup>187</sup>Os/<sup>188</sup>Os<sub>95Ma</sub> vary from 0.1131 to 0.1345, with most between 0.12 and 0.13, and no systematic differences are observed between MMS and basal harzburgites (Fig. 4a and Table 1). These values span nearly the entire global abyssal peridotite range (Becker and Dale, 2016), with the least radiogenic samples having Re-depletion model ages (T<sub>RD</sub>) ~2.2 Ga (using Primitive Upper Mantle (PUM) evolution curve of Meisel et al. (2001)). T<sub>RD</sub> ages are obtained by comparing measured <sup>187</sup>Os/<sup>188</sup>Os values directly with the mantle evolution curve, implicitly assuming Re concentration equals zero in residual peridotite after melt extraction. However, this assumption is often false, as moderate melt extraction leaves peridotites with non-zero Re contents. Therefore, T<sub>RD</sub> ages are always minimum values that could dramatically underestimate true melt extraction ages. Nevertheless, the T<sub>RD</sub> ages >0.5 Ga of most of the harzburgites imply that they experienced some melt extraction hundreds of million years before possible remelting beneath the Oman spreading center.

Dunites have highly variable compositions correlating with their structural contexts (Fig. 3, 4b-c):

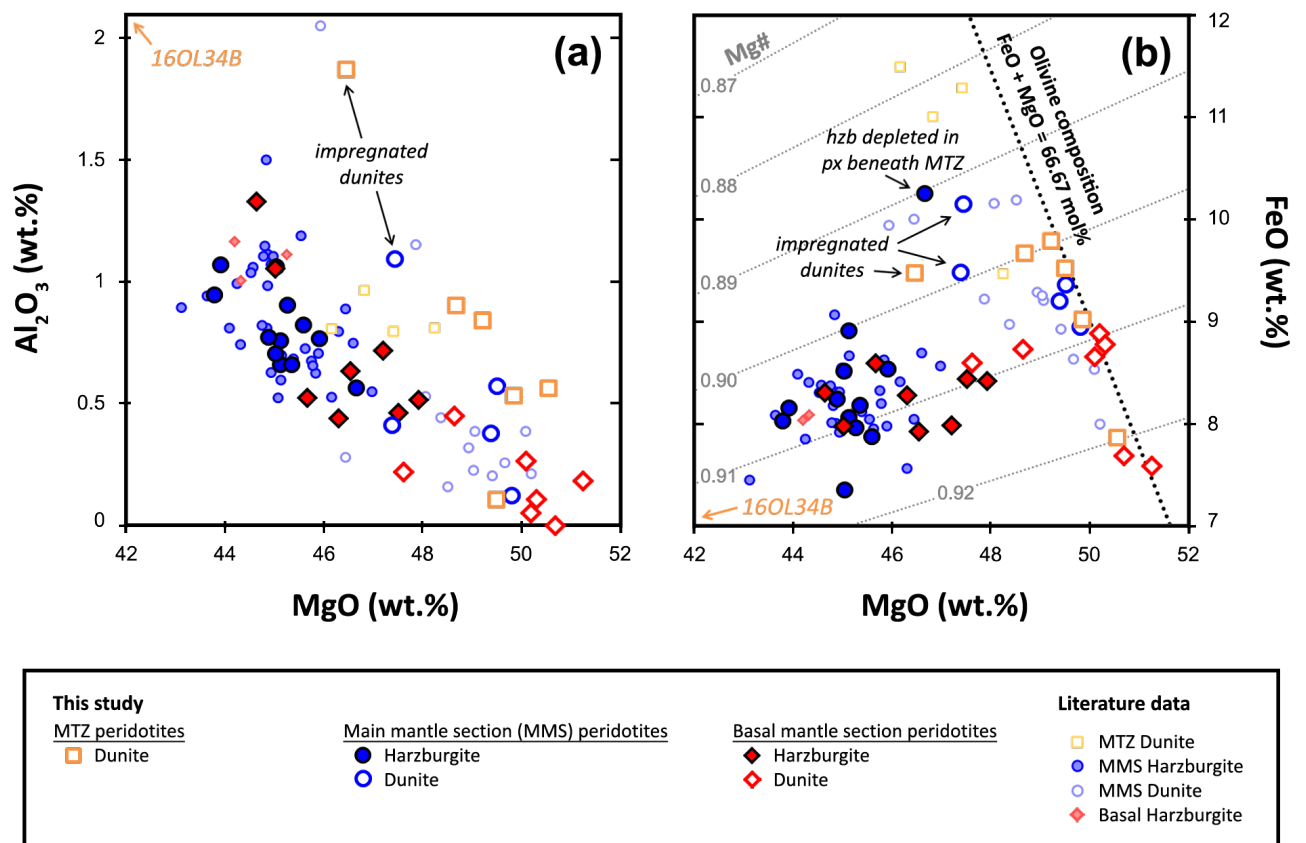
(1) MTZ dunites have generally low Mg# (0.897-0.920; mean: 0.904) with higher Al<sub>2</sub>O<sub>3</sub> (0.09-1.71 wt.%) and lower Os concentration (0.39 to 1.17 ppb) than most other dunites. Their <sup>187</sup>Os/<sup>188</sup>Os<sub>95Ma</sub> ratios (0.1415 to 0.1490) are higher than the estimated PUM value (~0.1289 at 95 Ma; Meisel et al. (2001)) and coherent with those of Oman MTZ chromitites (Ahmed et al., 2006). Plagioclase-impregnated dunite 10OM25 and especially troctolite 16OL34B are enriched in magmatophile elements (Fe, Al, Ca)

257 (Fig. 3). The Os concentration and  $^{187}\text{Os}/^{188}\text{Os}_{95\text{Ma}}$  of dunite 100M25 do not differ from those of other  
258 MTZ dunites, but troctolite 16OL34B is less radiogenic (0.1319) and has a higher Os concentration  
259 (2.30 ppb) (Fig. 4b).

260 (2) Relative to MTZ dunites, most MMS dunites display a restricted range of Mg# (0.893-0.908; mean:  
261 0.902), lower  $\text{Al}_2\text{O}_3$  (mostly 0.11-0.51 wt.%), higher Os concentration (1.12 to 5.95 ppb) and lower  
262  $^{187}\text{Os}/^{188}\text{Os}_{95\text{Ma}}$  (0.1249 to 0.1330). One unusual sample (16OD9A) located ~1 km below the MTZ has  
263 atypical Os characteristics (11.80 ppb Os;  $^{187}\text{Os}/^{188}\text{Os}_{95\text{Ma}} = 0.1483$ ) but an unexceptional major element  
264 composition (Mg# = 0.905;  $\text{Al}_2\text{O}_3 = 0.33$  wt.%). In MMS dunite/harzburgite pairs, the dunite is always  
265 much more radiogenic than the harzburgite (Fig. 4c).

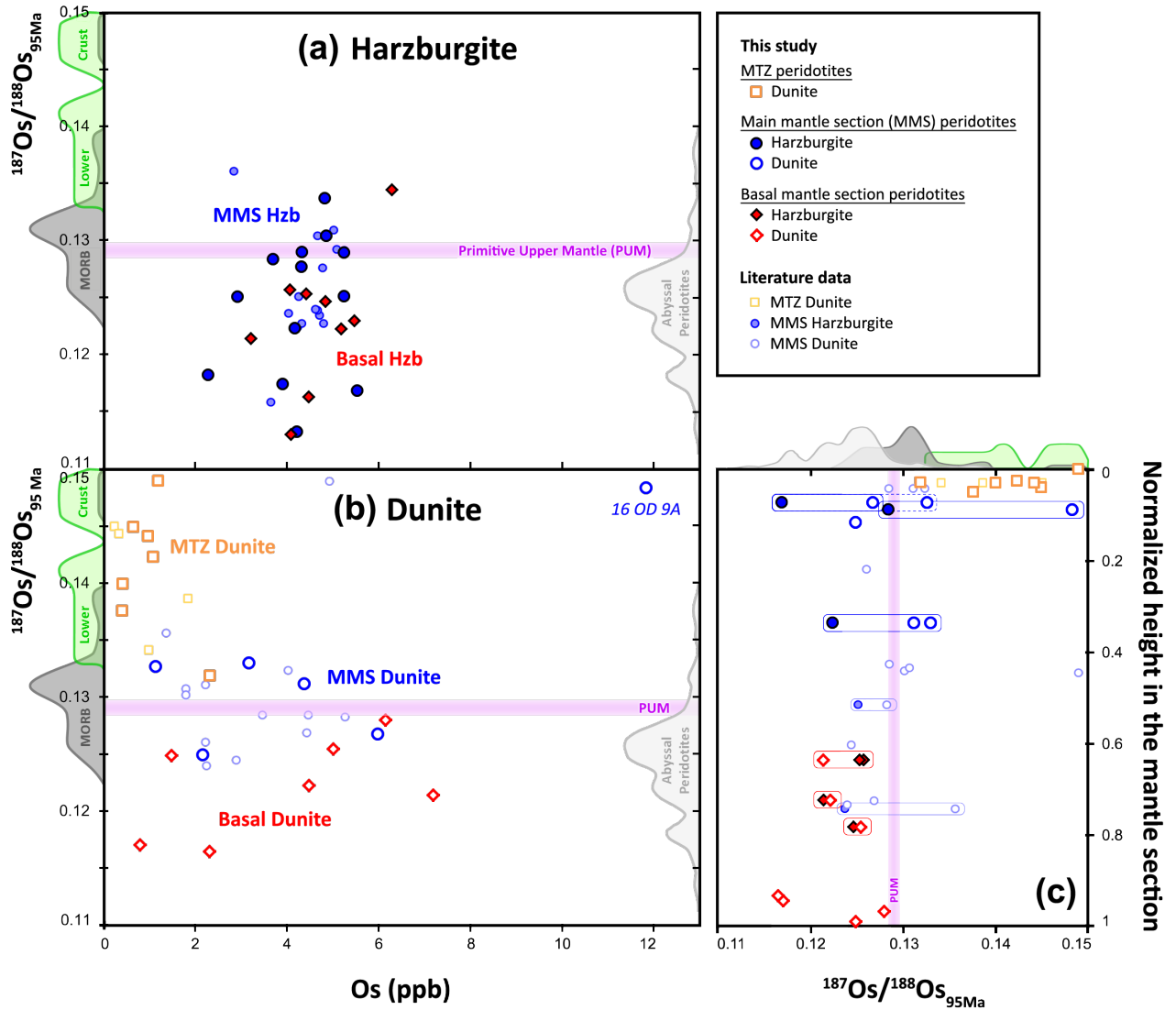
266 (3) Basal dunites display higher overall Mg# (0.908-0.923; mean: 0.914) and lower  $\text{Al}_2\text{O}_3$  ( $\leq 0.8$  wt.%)  
267 than the other dunites. Their Os concentrations vary substantially (0.77 to 7.17 ppb), while their  
268  $^{187}\text{Os}/^{188}\text{Os}_{95\text{Ma}}$  ratios (0.1165 to 0.1280) are similar to abyssal peridotite values. Unlike in the MMS,  
269 paired dunites and harzburgites collected in the BBU have very similar isotope ratios.

270 When placed in the structural framework defined here, previous Mg#,  $\text{Al}_2\text{O}_3$ , Os concentration and Os  
271 isotope results from harzburgites and dunites of the Oman ophiolite (Godard et al., 2000; Hanghøj et  
272 al., 2010; Senda et al., 2020; Xiong et al., 2020a,b) are consistent with these observations.



273

274 **Fig. 3.** Whole-rock major element compositions of harzburgites and the three types of dunite  
 275 recalculated on a volatile-free basis in **(a)**  $\text{Al}_2\text{O}_3$  vs.  $\text{MgO}$  and **(b)**  $\text{FeO}$  vs.  $\text{MgO}$  diagrams. In panel **(b)**,  
 276 dotted grey lines represent constant  $\text{Mg}\#$  values and the bold dotted black line shows the evolution of  
 277 olivine composition constrained by  $\text{FeO} + \text{MgO} = 66.67$  mol% following Godard et al. (2000). In all  
 278 panels, olivine troctolite (16OL34B) plots outside of the graph area, with higher  $\text{Al}_2\text{O}_3$  and lower  $\text{FeO}$   
 279 and  $\text{MgO}$  concentrations. Published Oman peridotite data are shown for comparison: MTZ dunites  
 280 (Godard et al., 2000); MMS dunites (Godard et al., 2000; Hanghøj et al., 2010); MMS harzburgites  
 281 (Godard et al., 2000; Hanghøj et al., 2010) and basal harzburgites (Godard et al., 2000). Attribution of  
 282 samples reported in the literature to the three domains defined in our study was based on their  
 283 geographic positions in the mantle section.



284

285 **Fig. 4.** Os isotope compositions of harzburgites and the three types of dunite. **(a)**  $^{187}\text{Os}/^{188}\text{Os}_{95\text{Ma}}$  vs.  
 286  $[\text{Os}]$  in harzburgites; **(b)**  $^{187}\text{Os}/^{188}\text{Os}_{95\text{Ma}}$  vs.  $[\text{Os}]$  in dunites; **(c)** Variation in dunite  $^{187}\text{Os}/^{188}\text{Os}_{95\text{Ma}}$  with  
 287 approximate height in the stratigraphic section, normalized to the total height (Moho to base) of each  
 288 section to allow comparison of samples from different cross-sections. Harzburgites taken adjacent to  
 289 six of the dunites are also shown, with blue and red contours delimiting harzburgite-dunite pairs in the  
 290 MMS and the BBU, respectively. Dunite 16OD4C (dashed blue contour) is associated with the  
 291 16OD4D<sub>Dun/Hzb</sub> pair but was collected at a greater distance from the harzburgite (30 cm). In all panels,  
 292 light purple fields represent the estimated  $^{187}\text{Os}/^{188}\text{Os}$  ratio for the Primitive Upper Mantle (PUM)  
 293 ( $\sim 0.1289$  at 95 Ma) (Meisel et al., 2001). Light grey, dark grey and green curves on both sides of the  
 294 diagrams show the probability density distributions of  $^{187}\text{Os}/^{188}\text{Os}$  ratios for abyssal peridotites  
 295 (compilation in Becker and Dale (2016)), MORB (MORB sulfide data compiled in Gannoun et al. (2016))

296 and Oman lower crust (Peucker-Ehrenbrink et al., 2012) respectively. Published Oman peridotite data  
 297 are shown for comparison: MTZ dunites (Xiong et al., 2020a,b); MMS dunites (Hanghøj et al., 2010;  
 298 Xiong et al., 2020a,b) and MMS harzburgites (Hanghøj et al., 2010) (symbols as in Fig. 3), with  
 299 attribution to each mantle domain based on geographic positions in the mantle section.

300 **Table 1.** Mg#, Re and Os concentrations and Os isotope compositions of the studied Oman peridotites

Sample	Massif	Lithology	Hzb/Dun pairs	Normalized height in the section	Mg#	[Os] (ppb)	[Re] (ppb)	<sup>187</sup> Re/ <sup>188</sup> Os	( <sup>187</sup> Os/ <sup>188</sup> Os) <sub>m</sub>	( <sup>187</sup> Os/ <sup>188</sup> Os) <sub>95 Ma</sub>	2σ error
<i>Moho Transition Zone (MTZ) peridotites</i>											
10 OM 25	Sumail (Maqsad)	impregnated dunite		0.030	0.897	0.399	0.114	1.376	0.14214	0.13996	0.00055
10 OM 45C	Sumail (Maqsad)	dunite		0.030	0.900	0.947	0.050	0.255	0.14456	0.14415	0.00064
18 OK 26	Sumail (Maqsad)	dunite		0.040	0.920	0.628	0.409	3.149	0.14993	0.14494	0.00086
10 OM 5C*	Sumail (Mansah)	dunite		0.025	0.908	1.063			0.14235	0.14115	0.00052
10 OM 5C-d							0.168	0.760			
07 OD 1	Sumail (Mansah)	dunite		0.050	0.900	0.390	0.199	2.462	0.14151	0.13761	0.00057
16 OL 11B	Wadi Tayin	pure dunite		0.000	0.903	1.173	0.033	0.137	0.14922	0.14900	0.00085
16 OL 34B	Wadi Tayin	olivine troctolite		0.028	0.899	2.305	0.053	0.111	0.13209	0.13192	0.00200
<i>Main mantle section (MMS) peridotites</i>											
16 OD 5C	Nakhl-Rustaq	depleted harzburgite		0.007	0.890	2.274	0.448	0.948	0.11976	0.11826	0.00199
16 OD 5D	Nakhl-Rustaq	harzburgite		0.007	0.916	4.211	0.152	0.174	0.11362	0.11334	0.00116
16 OD 7	Nakhl-Rustaq	harzburgite		0.053	0.909	2.921	0.025	0.042	0.12517	0.12510	0.00160
16 OD 4D <sub>Hzb</sub>	Nakhl-Rustaq	harzburgite	16 OD 4D <sub>Dun</sub>	0.073	0.900	5.519	0.358	0.312	0.11741	0.11691	0.00054
16 OD 9C	Nakhl-Rustaq	harzburgite	16 OD 9A	0.089	0.908	3.691	0.130	0.170	0.12871	0.12844	0.00134
16 OD 2	Nakhl-Rustaq	harzburgite		0.241	0.907	4.314	0.500	0.559	0.12990	0.12902	0.00114
16 OD 1A	Nakhl-Rustaq	harzburgite	16 OD 1B	0.337	0.906	4.164	0.599	0.693	0.12350	0.12241	0.00059
16 OD 10	Nakhl-Rustaq	harzburgite		0.419	0.906	4.855	0.381	0.378	0.13112	0.13052	0.00106
11 OD 15A	Sumail	harzburgite		0.280	0.912	3.894	0.152	0.187	0.11782	0.11753	0.00057
07 OD 24	Sumail	harzburgite		0.254	0.907	4.826	0.460	0.459	0.13451	0.13378	0.00051
07 OD 27B	Sumail	harzburgite		0.344	0.904	4.314	0.221	0.247	0.12817	0.12778	0.00052
07 OD 8C	Sumail	harzburgite		0.150	0.910	5.246	0.379	0.348	0.12961	0.12906	0.00066
07 OD 8C-d						5.228	0.321	0.295	0.12570	0.12523	0.00056
16 OD 4C	Nakhl-Rustaq	impregnated dunite (vein)	16 OD 4D <sub>Hzb</sub>	0.073	0.893	1.120	0.305	1.312	0.13474	0.13267	0.00106
16 OD 4D <sub>Dun</sub>	Nakhl-Rustaq	impregnated dunite (vein)	16 OD 4D <sub>Hzb</sub>	0.073	0.899	5.954	0.414	0.335	0.12729	0.12676	0.00055
16 OD 9A	Nakhl-Rustaq	pure dunite (band)	16 OD 9C	0.089	0.905	11.802	0.431	0.177	0.14862	0.14834	0.00063
16 OD 1B	Nakhl-Rustaq	dunite (vein)	16 OD 1A	0.337	0.904	3.145	0.087	0.134	0.13324	0.13303	0.00065
16 OD 1B-d						4.353	0.094	0.104	0.13135	0.13119	0.00061
16 OD 31	Wadi Tayin	dunite (band)		0.116	0.908	2.147	0.910	2.043	0.12814	0.12491	0.00215
<i>Basal peridotites</i>											
16 OD 13C	Nakhl-Rustaq	harzburgite	16 OD 13B	0.637	0.909	4.415	0.415	0.453	0.12607	0.12536	0.00054
16 OD 13C-d						4.076	0.379	0.448	0.12647	0.12577	0.00058
16 OL 25	Wadi Tayin	harzburgite		0.724	0.905	6.289	0.081	0.062	0.13464	0.13454	0.00088
16 OL 26B	Wadi Tayin	harzburgite	16 OL 26A	0.724	0.910	3.214	0.022	0.032	0.12151	0.12146	0.00148
16 OL 27B	Wadi Tayin	harzburgite	16 OL 27A	0.784	0.910	4.843	0.314	0.312	0.12522	0.12472	0.00107
16 OL 27C	Wadi Tayin	harzburgite		0.784	0.913	4.097	0.046	0.053	0.11314	0.11306	0.00121
16 OL 28B	Wadi Tayin	harzburgite		0.860	0.909	4.481	0.168	0.180	0.11659	0.11630	0.00113
16 OL 29	Wadi Tayin	harzburgite		0.872	0.906	5.187	0.169	0.157	0.12256	0.12231	0.00100
16 OL 24	Wadi Tayin	harzburgite		0.878	0.913	5.475	0.221	0.194	0.12335	0.12305	0.00097
16 OD 13B	Nakhl-Rustaq	dunite (band)	16 OD 13C	0.637	0.923	7.169	0.158	0.106	0.12155	0.12139	0.00054
16 OD 15E	Nakhl-Rustaq	dunite (band)		0.934	0.911	2.291	0.106	0.223	0.11688	0.11653	0.00070
16 OD 18B	Sumail	dunite (band)		0.969	0.908	6.134	0.018	0.014	0.12800	0.12798	0.00060
16 OD 19A	Sumail	pure dunite (band)		0.946	0.910	0.774	0.066	0.413	0.11773	0.11707	0.00120
16 OL 26A	Wadi Tayin	dunite (band)	16 OL 26B	0.724	0.909	4.460	0.014	0.015	0.12227	0.12225	0.00112
16 OL 27A	Wadi Tayin	dunite (band)	16 OL 27B	0.784	0.912	4.998	0.079	0.077	0.12560	0.12548	0.00102
14 11E	Haylayn	pure dunite (band)		0.990	0.922	1.474	0.157	0.512	0.12573	0.12492	0.00053

Os isotopic compositions in whole rock were analyzed at the CRPG laboratory in Nancy (France) using N-TIMS (Finnigan MAT 262) and MC-ICP-MS (Neptune +). All uncertainties are 2σ and include all recognized sources of uncertainty, including in-run analytical precision, reproducibility of standard analyses, uncertainties related to the variability of the blank and its isotope composition, uncertainties related to the age correction (95 Ma). Samples belonging to harzburgite/dunite pairs collected in close proximity (<1 meter) are indicated. For each sample, an approximate estimation of its height in the mantle section was obtained by normalizing to the total section height to compare samples from different cross-sections. Duplicate analyses were performed for several samples (noted "-d") and UB-N standard. More details are presented in the Supplementary Material.

\* For 10 OM 5C sample, (<sup>187</sup>Os/<sup>188</sup>Os)<sub>95 Ma</sub> was calculated using Re compositions of its duplicate.  
 Mg# = Mg/(Mg+Fe)at; Hzb = harzburgite; Dun = dunite.

## 302 5. Discussion

303 Our coupled geochemical and structural observations underscore three findings:

304 (1) Throughout the mantle section, harzburgite Mg#, Al<sub>2</sub>O<sub>3</sub> contents, Os concentrations and isotopic  
305 compositions span a range comparable to that of abyssal peridotites (Becker and Dale, 2016) (Fig. 3,  
306 4a). Dunites display more variable compositions linked to their structural contexts, with <sup>187</sup>Os/<sup>188</sup>Os<sub>95Ma</sub>  
307 and Al<sub>2</sub>O<sub>3</sub> content increasing and Mg# generally decreasing from the BBU through the MMS to the  
308 MTZ (Fig. 3, 4b-c).

309 (2) In the BBU, dunite Os isotope compositions closely resemble those of adjacent harzburgites (Fig.  
310 4c). In contrast, dunites in the overlying MMS have more radiogenic compositions than associated  
311 harzburgites.

312 (3) In the MTZ, dunite <sup>187</sup>Os/<sup>188</sup>Os<sub>95Ma</sub> ratios are much more radiogenic than those of abyssal  
313 peridotites or even MORB (Gannoun et al., 2016), and dunite Os concentrations are low (Fig. 4b-c).

### 314 5.1. Evidence against seawater contamination

315 We first consider whether the radiogenic compositions of the MTZ dunites result from hydrothermal  
316 circulation of seawater, which has high <sup>187</sup>Os/<sup>188</sup>Os (~0.51–0.57 in the mid-Cretaceous; Ravizza et al.  
317 (2001)) and could modify <sup>187</sup>Os/<sup>188</sup>Os in oceanic peridotites (discussion in Becker and Dale (2016)).  
318 Given the very low Os concentration of seawater (~10 fg/g; Levasseur et al. (1998)), water/rock ratios  
319 required to significantly change Os compositions of peridotites are extremely high (>1000). In  
320 ophiolitic peridotites, water/rock ratios are almost always <100 (McCulloch et al., 1981), so significant  
321 modification of <sup>187</sup>Os/<sup>188</sup>Os should be rare.

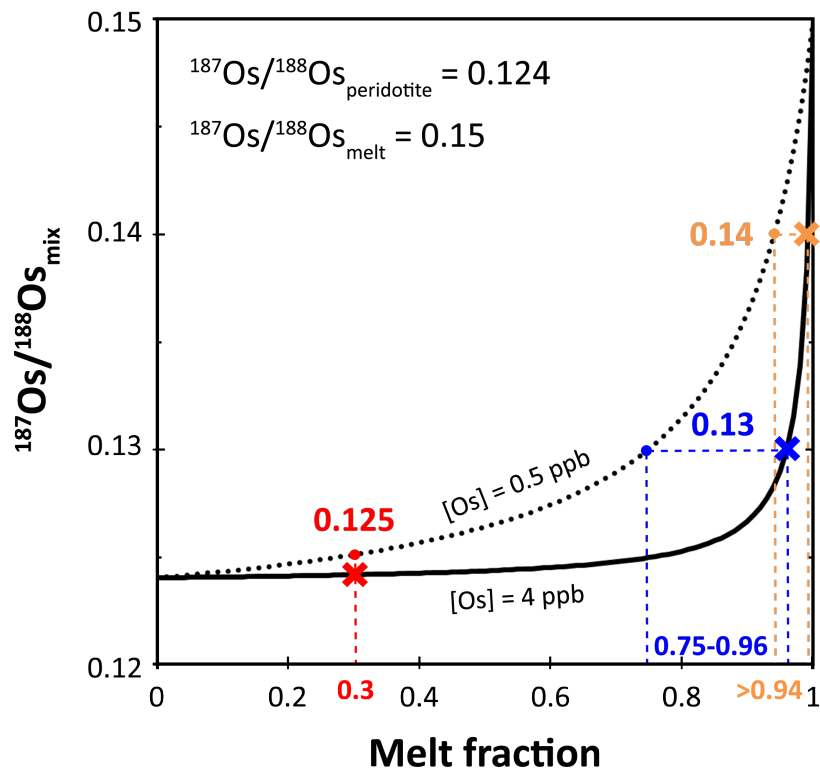
322 Our samples have water contents (LOI < 15.42%, most <12%) typical of serpentinized peridotites. No  
323 correlation is observed between LOI values, highly mobile element (Rb, Cs, Ba and U) abundances or  
324 Th/U ratios (Fig. A.2 and Tables A.3-4) and Os isotope composition. As shown in Fig. A.2b, interaction  
325 of typical peridotite (<sup>187</sup>Os/<sup>188</sup>Os = 0.124; [Os] from 0.4 to 6 ppb) with seawater cannot produce the  
326 radiogenic Os compositions found in MTZ dunites without decreasing Th/U ratios far below observed  
327 levels, implying that the Os isotope signatures of our samples reflect essentially magmatic processes.

328 **5.2. Os isotope evolution during melt-rock interaction**

329 **5.2.1. First order considerations**

330 Dunite bodies are generally viewed as reaction products formed as melts migrate through host  
331 harzburgite, dissolving pyroxene and precipitating olivine. Focused melting experiments show that  
332 melt fractions of 0.25-0.30 are required to dissolve all pyroxenes at 0.5 GPa (Lambart et al., 2009).  
333 However, once all pyroxenes have been removed, the amount of additional melt migrating through a  
334 dunite body is difficult to quantify. Signatures of incompatible element tracers, which are dramatically  
335 less abundant in dunite than in melt, will be rapidly overprinted by equilibration with the liquid during  
336 melt percolation. In contrast, peridotites, including dunites, have higher Os concentrations than  
337 mantle melts. Thus, as melts equilibrate with peridotite during melt percolation, dunite Os  
338 concentration and  $^{187}\text{Os}/^{188}\text{Os}$  should change slowly and progressively, allowing this element to serve  
339 as a tracer of the extent of melt-peridotite interaction.

340 To roughly estimate the proportion of melt needed to obtain the initial isotopic compositions of the  
341 three types of dunite, we first consider a two-component mixture between peridotite ( $^{187}\text{Os}/^{188}\text{Os}=$   
342 0.124, typical of Oman harzburgites) and melt (0.2 ppb Os;  $^{187}\text{Os}/^{188}\text{Os}= 0.150$ ). The melt  $^{187}\text{Os}/^{188}\text{Os}$   
343 was chosen to be slightly more radiogenic than the MTZ dunites. This value is higher than those of all  
344 MORB and most arc lavas (except for extrusives with extremely low Os contents, whose isotope  
345 compositions are easily modified by assimilation of radiogenic crustal material; see data compilation in  
346 Bezard et al. (2021)). Results are shown for two peridotite Os concentrations (Fig. 5; details in  
347 [Supplementary Material](#)), representing typical harzburgite (4 ppb) and MTZ dunite (0.5 ppb). The  
348 peridotite  $^{187}\text{Os}/^{188}\text{Os}$  ratio rises slowly with increasing melt fraction and is nearly unchanged at the  
349 melt fraction (0.25-0.30) needed to fully transform harzburgite to dunite. Much higher melt fractions,  
350 0.75-0.96 and  $\geq 0.94$  respectively using the assumed parameters, are needed to attain  $^{187}\text{Os}/^{188}\text{Os}$   
351 values of MMS ( $\sim 0.130$ ) or MTZ ( $\sim 0.140$ ) dunites.



352

353 **Fig. 5.** Two-component mixture between peridotite ( $^{187}\text{Os}/^{188}\text{Os} = 0.124$ ) and melt ( $^{187}\text{Os}/^{188}\text{Os} = 0.150$ ;  
 354  $[\text{Os}] = 0.2 \text{ ppb}$ ) (cf. [Supplementary Material](#)). The two starting Os concentrations for the peridotite are  
 355 used to simulate a mixture of a typical harzburgite (4 ppb; continuous curve) and of a MTZ dunite (0.5  
 356 ppb; dotted curve) with the melt. Basal dunites (red) have Os isotope compositions similar to those of  
 357 harzburgites, suggesting low melt fractions. Higher melt fractions, 0.75-0.96 and  $\geq 0.94$  respectively,  
 358 increase  $^{187}\text{Os}/^{188}\text{Os}$  to 0.130 (MMS dunite; blue) or 0.140 (MTZ dunite; orange).

359

## 5.2.2. Melt-rock interaction during melt percolation

360

### 5.2.2.1. *Single-cell percolation model*

361

While two-component mixing models allow qualitative assessment of the melt fractions needed to

362

produce the radiogenic compositions of MMS and MTZ dunites, melt percolation models taking the Os

363

partition coefficients ( $k_d$ ) of the pertinent phases into account are more realistic. One critical point is

364

the compatible behavior of Os in common mantle rocks partly due to its extremely chalcophile nature

365

( $k_{d \text{ in sulfide}} \sim 10^6$ ) (Mungall and Brenan, 2014). During percolation of sulfide-undersaturated melts in the

366

uppermost mantle, the sulfide fraction in the peridotite decreases progressively. As long as the

367

peridotite contains sulfide, Os is trapped in the residue. When the peridotite loses its final trace of

368

sulfide, the Os partition coefficient of the peridotite is likely to be lowered significantly causing Os

369

concentration to decrease with continuing melt percolation. Concomitantly, if the percolating melts

370

have a more radiogenic composition, the  $^{187}\text{Os}/^{188}\text{Os}$  of the host peridotite increases gradually.

371

In a simple model, a representative elementary volume (cell) of harzburgite is flushed repeatedly by

372

increments of 2% melt of a constant radiogenic composition (details in [Supplementary Material](#)). As in

373

most more complex models (e.g. Vernières et al. (1997)), chemical and isotopic equilibrium with the

374

peridotite is assumed to be attained after each melt increment is added. After equilibration, the melt

375

moves out of the cell and is replaced by fresh melt of the original composition. We suppose that the

376

initial Os compositions of melt and harzburgite are the same as those used in the two-component

377

mixture, and that transformation of harzburgite to dunite occurs after interaction with 25-30% of

378

melt, corresponding to 10-15 melt increments. For simplicity, we also consider that complete sulfide

379

removal is coincident with full transformation of harzburgite into dunite, i.e. when opx depletion is

380

complete. If sulfide exhaustion occurs slightly before or after transformation to dunite, the results will

381

not change substantively. In our model, the harzburgite contains 100 ppm sulfide, equivalent to ~40

382

ppm S, assumed to decrease to zero over 10 increments of 2% melt.

383

After each increment of new melt equilibrates with the peridotite, the Os isotope composition is

384

controlled by mass balance, while the new Os concentrations of the melt and the residual peridotite

385 are controlled by the Os partition coefficients of the phases present. Osmium is strongly retained by  
386 the residue as long as sulfides remain. As sulfur is removed into the silicate melt, the IPGE (Iridium-  
387 group PGE: Os, Ir, Ru, Rh) are increasingly concentrated in the refractory sulfide residues, leading  
388 eventually to exsolution of platinum group minerals (PGM) such as Ir-Os alloys (Fonseca et al., 2012).  
389 Ir-Os alloys, laurites ( $\text{RuS}_2$ ) and other PGM are probably the main hosts of Os in dunites and other  
390 sulfide-poor mantle peridotites (reviewed in Lorand and Luguet (2016) and O'Driscoll and González-  
391 Jiménez (2016)). In addition to PGM, experimental data (summarized in Brenan et al. (2016)) indicate  
392 that Ir and Ru are compatible in Cr-rich spinel, which constitutes ~1-3% of the dunite (Table A.2), and  
393 to a lesser extent in olivine, suggesting that Os could also be hosted by these phases. Thus, Os may  
394 behave as a moderately compatible element in dunite even after all sulfides have been removed.  
395 Nevertheless, dunites that have been fluxed by large quantities of magma have lower Os  
396 concentrations than most mantle harzburgites (Büchl et al., 2002), suggesting unsurprisingly that the  
397 compatibility of Os in peridotite is lowered in the absence of sulfide. Taking these observations into  
398 consideration, we consider a bulk partition coefficient ( $D_{\text{Os}}$ ) of 2 for dunites, which are assumed to  
399 have lost all of their original sulfide content. The effect of varying this value is explored below. Further  
400 constraint of  $D_{\text{Os}}$  will require a better understanding of the behavior and stability of Os-bearing PGM  
401 during melt fluxing.

402

### 5.2.2.2. Results for the three types of dunite in the model framework

403

Results of the model are compared with the data in Fig. 6. The model is obviously simplistic. The

404

harzburgitic protolith is treated as a single composition rather than the wide range of harzburgite

405

compositions observed in the ophiolite, likely explaining much of the mismatch with the data.

406

Similarly, incoming melt composition and  $D_{Os}$ , treated as constants, most probably vary with time.

407

Nevertheless, this model provides a conceptual framework for examining the extent of melt-rock

408

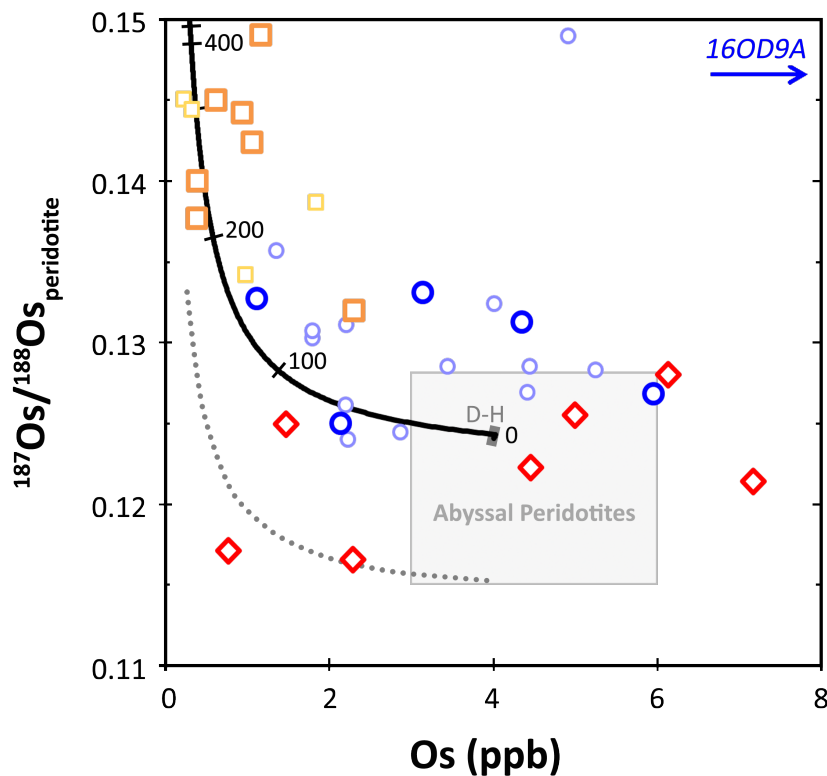
reaction experienced by each type of dunite. While the geometries and contexts of the three types of

409

dunite are quite different, the melt-rock reaction process can be modeled in each case by melt fluxing

410

through a volume of rock, using the parameters given in the caption to Fig. 6.



411

412

**Fig. 6.** Effect of percolation of radiogenic melt ( $^{187}\text{Os}/^{188}\text{Os} = 0.150$ ;  $[\text{Os}] = 0.2$  ppb) through a

413

representative elementary volume (i.e., a single cell) of typical harzburgite ( $^{187}\text{Os}/^{188}\text{Os} = 0.124$ ;  $[\text{Os}] = 4$

414

ppb). Black curve shows evolution of peridotite  $^{187}\text{Os}/^{188}\text{Os}$  vs.  $[\text{Os}]$  during this process. As repeated

415

increments of melt (taken here as 2%) traverse the harzburgite, the pyroxenes will dissolve

416

progressively, resulting in dunite formation after ~10-15 increments have passed (zone indicated as D-

417

H on diagram). Concomitantly, any sulfides present in the harzburgite will also be dissolved in the

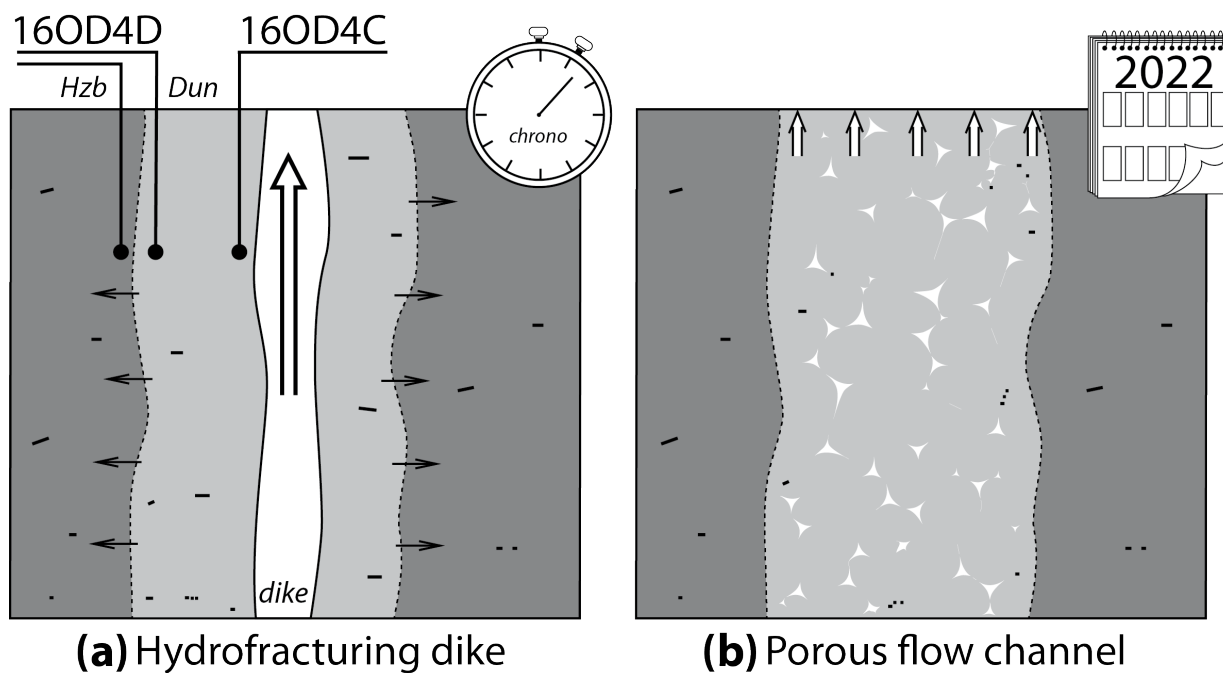
418 *percolating melt, with complete sulfide dissolution assumed to approximately coincide with the*  
419 *transition from harzburgite to dunite. As Os will be retained as long as sulfide is present, Os*  
420 *concentrations will not start to decrease before this transition is nearly complete. In the example*  
421 *shown, the starting harzburgite is assumed to contain 100 ppm sulfide (~40 ppm S),  $k_{d,Os} = 10^6$  for*  
422 *sulfide and  $D_{Os} = 2$  for dunite (see discussion of parameter choices in text and [Supplementary Material](#)).*  
423 *After transition to dunite, continued fluxing with repeated increments of melt (tick marks placed at*  
424 *100, 200, 300 and 400 increments on the curve) will cause the Os isotopic ratio and concentration to*  
425 *move from the starting position in the abyssal peridotite field along the black curve towards the higher*  
426  *$^{187}\text{Os}/^{188}\text{Os}_{95\text{Ma}}$  ratios and lower Os concentrations found in the MTZ dunites. Dotted grey curve*  
427 *represents percolation of a different melt ( $[\text{Os}] = 0.2$  ppb; MORB-like  $^{187}\text{Os}/^{188}\text{Os} = 0.133$  - Gannoun et*  
428 *al. (2016)), interacting with harzburgite with  $^{187}\text{Os}/^{188}\text{Os}$  towards the bottom of the abyssal peridotite*  
429 *range (Becker and Dale, 2016), possibly explaining low  $[\text{Os}]$  and unradiogenic compositions of two of*  
430 *the basal dunites. Os concentrations and initial Os isotope ratios for the three types of dunite are*  
431 *shown for comparison with the results of the melt percolation model (symbols as in [Fig. 3](#)).*

432 In the MTZ, about 300 increments of melt fluxing, equivalent to a melt/rock ratio  $\sim 6$ , would be needed  
433 to lower the Os contents and raise the  $^{187}\text{Os}/^{188}\text{Os}$  ratios of the initial harzburgite to the values ( $\sim 0.2$ -  
434  $1.0$  ppb and  $^{187}\text{Os}/^{188}\text{Os}_{95\text{Ma}} \sim 0.138$ - $0.149$ ) observed in MTZ dunites. Such high melt/rock ratios are  
435 consistent with the intense melt-peridotite interactions thought to occur in this zone (Boudier and  
436 Nicolas, 1995; Rospabé et al., 2018).

437 In the underlying MMS, nearly all dunites have  $^{187}\text{Os}/^{188}\text{Os}_{95\text{Ma}}$  in the range of  $0.125$ - $0.133$ , and in each  
438 pair studied, the dunites are more radiogenic than the associated harzburgite. For the same melt  
439 composition, the degree of melt-rock interaction required to obtain MMS-like Os isotopic signatures is  
440 smaller than for MTZ dunites (less than 150 increments of melt, corresponding to melt/rock ratios  $< 3$ ;  
441 [Fig. 6](#)). This is consistent with dunite formation by wall-rock reaction in melt dikes traversing the MMS  
442 ([Fig. 2b, 7a](#)), a process reported in other peridotitic bodies (Becker et al., 2001; Büchl et al., 2002).  
443 Wall-rock reaction would not have significantly modified the composition of melt flowing rapidly

444 through the center of the dike, because of the limited contact with the peridotite relative to the large  
445 volume of melt. In one case, two dunites were collected in the reaction zone of the same dike. Dunite  
446 16OD4C, sampled ~30 cm from the dike edge and impregnated with plagioclase and clinopyroxene,  
447 has a moderately radiogenic  $^{187}\text{Os}/^{188}\text{Os}_{95\text{Ma}}$  ratio (0.1327). Clinopyroxene-impregnated dunite  
448 16OD4D<sub>Dun</sub>, from the border with the host harzburgite (16OD4D<sub>Hzb</sub>), is less radiogenic (0.1268),  
449 suggesting lesser degrees of melt-rock interaction than near the dike center (Fig. 7a). This dunite is  
450 nevertheless more radiogenic than the harzburgite (0.1169). The unusual MMS dunite band 16OD9A,  
451 with very high Os concentration (11.80 ppb) and very radiogenic  $^{187}\text{Os}/^{188}\text{Os}_{95\text{Ma}}$  (0.1483) cannot be  
452 explained by this model and instead requires a specific mechanism of PGM or radiogenic sulfide  
453 precipitation. The Os isotopic composition of this sample is similar to the melt end-member used in  
454 the model, suggesting that such phases could have precipitated from magmas similar to those that  
455 interacted with harzburgite to form the MTZ and MMS dunites.

456 Individual basal dunites show Os isotope compositions in the abyssal peridotite range, indicating that  
457 each experienced much lower extents of melt-rock interaction than MTZ or MMS dunites (<<100 melt  
458 increments; Fig. 6), though, given the high proportion of dunite, the total melt flow through the BBU  
459 may have been quite high. Unlike the MMS dunites, BBU dunites have  $^{187}\text{Os}/^{188}\text{Os}_{95\text{Ma}}$  ratios very  
460 similar to those of adjacent harzburgites (Fig. 4c). They also have higher Mg#s and lower Al<sub>2</sub>O<sub>3</sub>  
461 contents than MMS and MTZ dunites (Fig. 3), arguing for lesser degrees of interaction with fertile  
462 melt. Furthermore, some sections include opx-bearing dunite and/or opx-poor harzburgite bands,  
463 likely formed by small degrees of melt-rock interaction insufficient to fully dissolve orthopyroxene.  
464 Two dunites have low Os concentrations coupled with very unradiogenic compositions, implying  
465 formation from harzburgites with very low  $^{187}\text{Os}/^{188}\text{Os}$  (though within the abyssal peridotite range)  
466 and perhaps interaction with less radiogenic melts than those required for MTZ dunites.



467 **(a)** Hydrofracturing dike **(b)** Porous flow channel

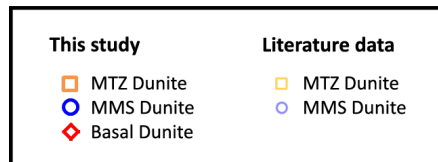
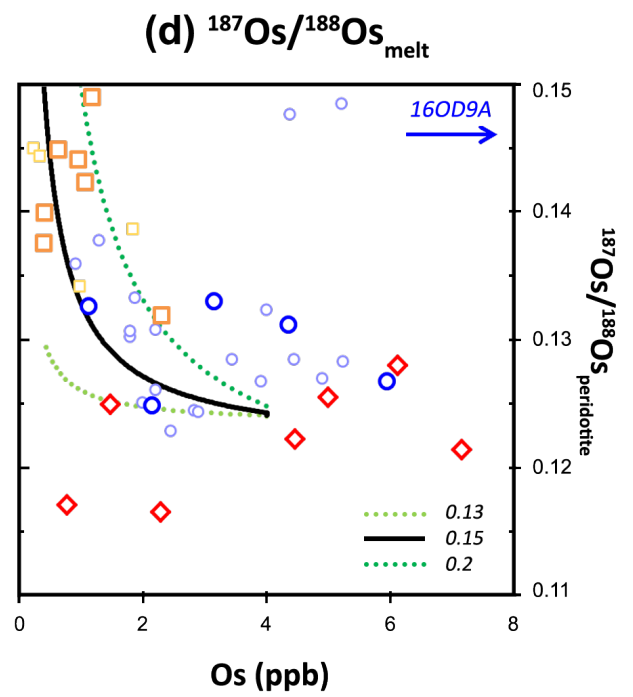
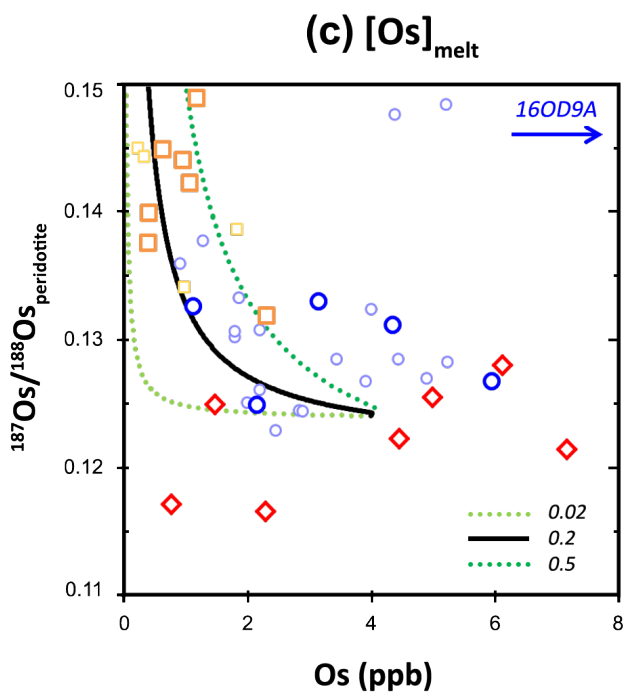
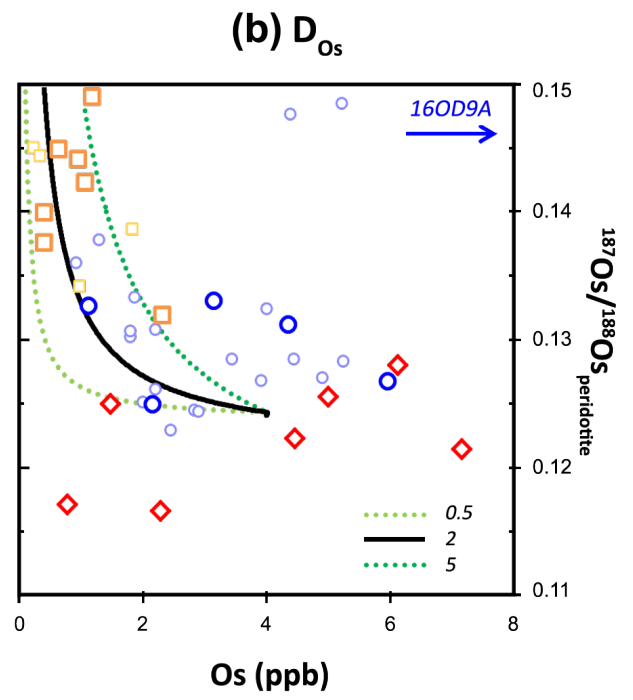
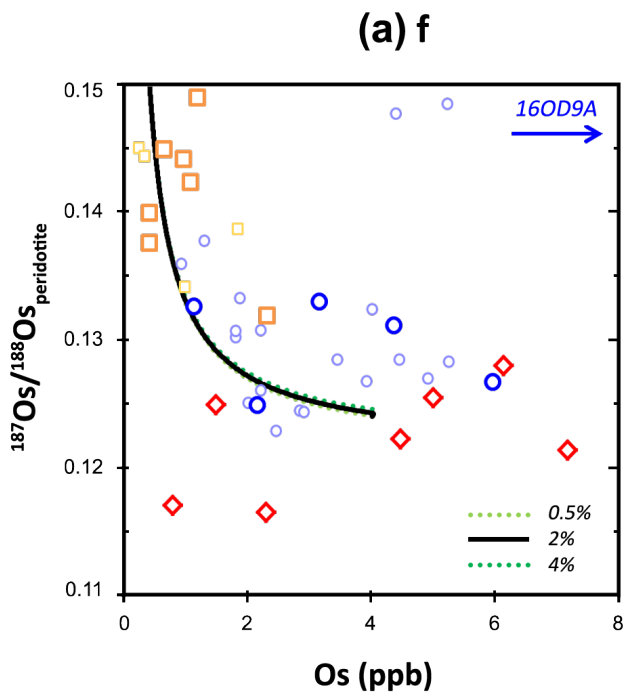
468 **Fig. 7.** Schematic diagrams of two end-member melt transport mechanisms: hydrofracturing **(a)** vs.  
 469 porous flow **(b)**. White: melt; light grey: dunite; dark grey: harzburgite; small black lines: spinel grains  
 470 marking the foliation. In panel **(a)**, a hydrofracturing dike contains 100% melt which travels fast (large  
 471 arrow) and has a short life-span (weeks or months). Dikes produce a dunite reaction zone at their  
 472 margins, that grows with time, and where the trace of foliation is preserved. In this case, samples at  
 473 the center of the reaction zone (ie, closer to the dike) may have reacted with melt for a longer time and  
 474 be more radiogenic than samples near the outside border of the reaction zone. This fits observations  
 475 for MMS dunite samples 16OD4D<sub>Dun</sub> and 16OD4C, both associated with host harzburgite 16D4D<sub>Hzb</sub>. In  
 476 panel **(b)**, a porous flow channel is represented with a homogeneous distribution of 1-3% melt, which  
 477 travels slowly through the solid matrix along grain boundaries (short arrows) and has a long life-span  
 478 (possibly steady-state). In this case, the dunite may fully equilibrate with the melt.

479

### 5.2.2.3. Insensitivity to parameter choices

480 The pertinence of the model parameter choices was evaluated by changing each parameter  
481 individually while holding the others constant (Fig. 8). The instantaneous melt fraction modifies the  
482 number of melt increments needed to obtain a given  $^{187}\text{Os}/^{188}\text{Os}$  ratio, but has little effect on the  
483 corresponding melt/rock ratio (Fig. A.3) or on the relationship between  $^{187}\text{Os}/^{188}\text{Os}$  and [Os] (Fig. 8a).  
484 The Os bulk-rock partition coefficient after sulfide exhaustion affects the rapidity with which Os in the  
485 dunite is lost to the passing melts, and accordingly the rate at which  $^{187}\text{Os}/^{188}\text{Os}$  is modified by  
486 repeated introduction of new melt (Fig. 8b and Fig. A.4). As discussed above, this parameter depends  
487 on the behavior and stability of rare PGM, and though modeled as a constant, probably changes  
488 during melt fluxing. To match both the Os isotope compositions and concentrations of the MTZ  
489 dunites,  $D_{\text{Os}}$  values between about 0.5 and 5 are required (Fig. 8b). For input melt of a fixed Os isotope  
490 composition, the Os concentration will control the number of iterations required to obtain a given  
491  $^{187}\text{Os}/^{188}\text{Os}$  ratio. The data field can be matched by melt Os concentrations ranging from about 0.02 to  
492 0.5 ppb (Fig. 8c and Fig. A.5). To produce MTZ dunites, the starting melt must have a  $^{187}\text{Os}/^{188}\text{Os}$  ratio  
493 of at least 0.15 (Fig. 8d and Fig. A.6), but melts with much higher ratios do not fit the data. The  
494 reasonableness of all of the successful parameters supports the plausibility of the model.

495 **Fig. 8.** Effect of varying (a) instantaneous melt fraction ( $f$ ) (0.5%, 2% and 4%), (b) Os bulk partition  
496 coefficient for dunite ( $D_{\text{Os}}$ ) (0.5, 2, 5), (c) melt Os concentration (0.02, 0.2 and 0.5) and (d) melt  
497  $^{187}\text{Os}/^{188}\text{Os}$  (0.13, 0.15 and 0.2) on [Os] and  $^{187}\text{Os}/^{188}\text{Os}$  of the peridotite in the single-cell melt  
498 percolation model shown in  $^{187}\text{Os}/^{188}\text{Os}$  vs. Os diagrams similar to Fig. 6. Data from our study for the  
499 three types of dunite, as well as published Oman dunite data are shown for comparison with initial Os  
500 isotope ratios (MTZ dunites - Xiong et al. (2020a,b); MMS dunites - Hangehøj et al. (2010) and Xiong et  
501 al. (2020a,b); attribution of literature data to dunite types based on geographic positions) (symbols as  
502 in Fig. 3). The chosen parameters in the model (black continuous curves) best fit the data.



503  
504

### 5.3. Need for rapid transport of radiogenic melt through the mantle section

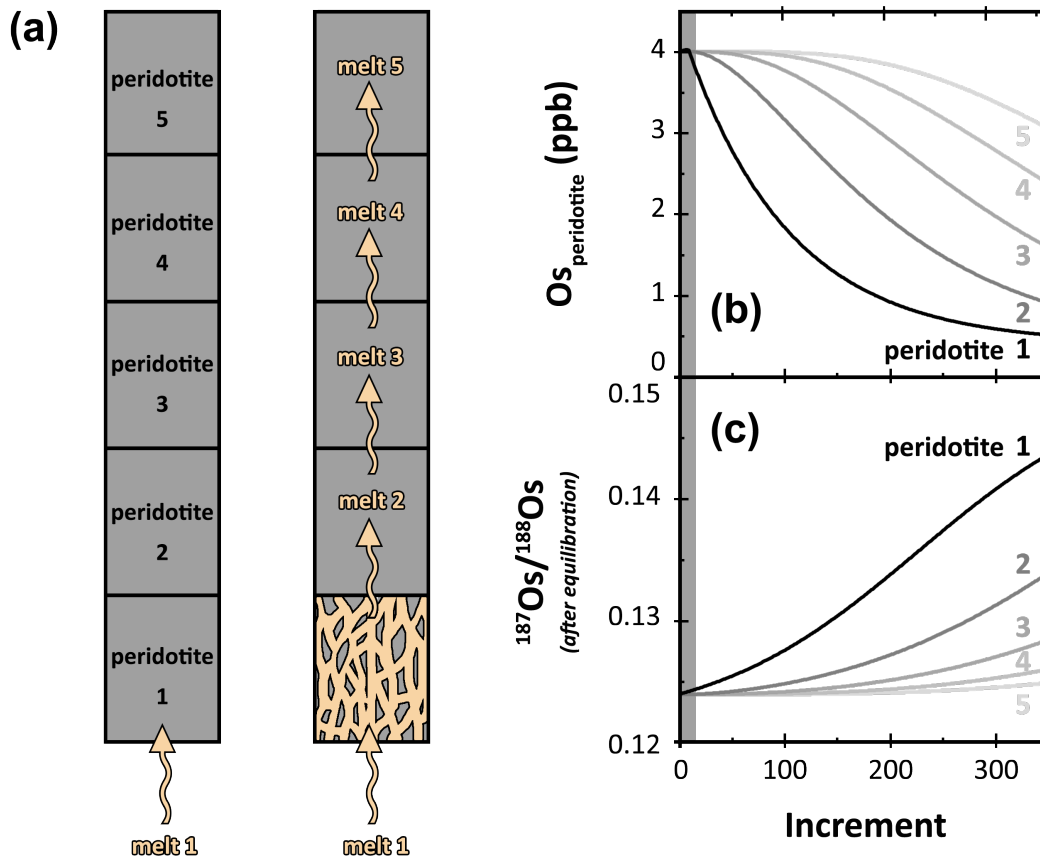
505  
506 A melt more radiogenic than MORB is needed to explain the radiogenic character of many MMS and  
507 nearly all MTZ dunites. The high  $^{187}\text{Os}/^{188}\text{Os}_{95\text{Ma}}$  ratios of the MTZ dunites are in good agreement with  
508 the  $^{187}\text{Os}/^{188}\text{Os}_{95\text{Ma}}$  ( $\sim 0.142$ ) of the Oman lower crust (Peucker-Ehrenbrink et al., 2012). Two sources of  
509 radiogenic melt are possible: ancient recycled oceanic crust (cf. pyroxenites; Sergeev et al. (2014)) or a  
510 downgoing slab (Becker et al., 2004). We cannot exclude either possibility, but the first case would  
511 require an unusual concentration of ancient pyroxenites in the mantle source, probably  
512 unrepresentative of heterogeneity in the upper mantle, as radiogenic values similar to those of MTZ  
513 dunites are rare in MORBs (Fig. 4). A slab-related source (effective during the main accretion phase of  
514 the Oman oceanic crust) seems more consistent with a suprasubduction setting for the Oman  
515 ophiolite, as proposed by Guilmette et al. (2018) and MacLeod et al. (2013). Regardless of its origin,  
516 the radiogenic nature of the melt is fortunate, as this allows us to trace the extent of melt-rock  
517 reaction in the different types of dunite.

518 A mechanism is needed to transport the radiogenic melt to the upper MMS and the MTZ. In one  
519 commonly accepted model (Kelemen et al., 1995), the melt is transported by porous flow in dunite  
520 channels. Once the olivine-rich channels are established, the melt is protected from equilibration with  
521 the surrounding peridotite, but equilibrates with the dunite through which it travels (Fig. 7b). To  
522 consider whether this mechanism is consistent with our Os results, we model a dunite channel as a  
523 stack of reaction cells, each similar to that described above (Fig. 9a and details in [Supplementary](#)  
524 [material](#)). Each increment of fresh radiogenic melt enters the bottom cell and equilibrates with the  
525 peridotite, and then migrates upwards into the overlying cell and is replaced by a new melt increment  
526 with the original composition. In this idealized model, the melt leaving this bottom cell will have a  
527 much less radiogenic Os composition than the entering melt, because of the strong buffering effect of  
528 the Os-rich peridotite (Fig. 9b). Similarly, the  $^{187}\text{Os}/^{188}\text{Os}$  ratios of the overlying cells will be  
529 successively less affected by melt interaction, with the ratio of the uppermost cell being hardly  
530 modified at all (Fig. 9c). Therefore, melt leaving the dunite channel will have a  $^{187}\text{Os}/^{188}\text{Os}$  ratio close  
531 to that of the original harzburgite from which the dunite formed (Fig. 9c). This implies that melts that

532 have traveled through such channels, equilibrating with the dunite along the way, cannot retain the  
533 highly radiogenic compositions needed to explain the high  $^{187}\text{Os}/^{188}\text{Os}_{95\text{Ma}}$  ratios of the MTZ dunites  
534 and the overlying lower crust. Instead, a mechanism without (or with little) equilibration with dunite  
535 or harzburgite is needed to bring melts with a radiogenic Os signature from depth towards the Moho.  
536 This lack of equilibration suggests rapid transfer of large melt volumes through the upper mantle  
537 section, also proposed by Kogiso et al. (2004) to explain the existence of linear correlations between  
538 Os and Sr, Nd and Pb isotopes in some ocean island basalts. The quantitative constraint that  
539 preservation of radiogenic Os compositions places on melt migration rates will depend on the  
540 geometry of melt pathways and on Os diffusion coefficients. While there are few experimental  
541 constraints on the latter, on theoretical grounds, Kogiso et al. (2004) estimated Os diffusion  
542 coefficients in olivine to be similar to those of Sr and Pb.

543 In addition to the melt brought to the MTZ through a rapid process, some melt may have percolated  
544 through the harzburgite in mantle diapirs (Godard et al., 2000; Lorand et al., 2009). Coexistence of two  
545 transport processes could be consistent with modeling of melt migration beneath mid-ocean ridges  
546 based on U-series isotope systematics (Elkins et al., 2019). However, any melt percolating slowly  
547 through harzburgite will acquire the non-radiogenic isotope composition of the peridotite, of which no  
548 trace is found in the MTZ dunites. Such a scenario would require the melts traveling rapidly to have  
549 had an even more radiogenic composition before mixing in the MTZ with melts that may have traveled  
550 slowly.

peridotite : [Os] = 4 ppb and  $^{187}\text{Os}/^{188}\text{Os} = 0.124$



551 melt 1 : [Os] = 0.20 ppb and  $^{187}\text{Os}/^{188}\text{Os} = 0.15$

552 **Fig. 9.** Multi-cell model (see text) showing Os evolution during melt percolation through dunite channel  
 553 developed in harzburgite. Starting Os compositions and sulfide fractions for harzburgite and melt are  
 554 the same as those in Fig. 6. Panel (a) depicts melt percolation through a five-cell peridotite column.  
 555 Melt enters the bottom cell and equilibrates with peridotite. After equilibration the melt and peridotite  
 556 will have the same isotopic composition. The melt then moves into the overlying cell as a fresh melt  
 557 increment enters the bottom cell; this process continues up the column. Compositions of peridotite cells  
 558 (black to light grey curves) vs. melt increment are shown in (b) [Os] and (c)  $^{187}\text{Os}/^{188}\text{Os}$ ; grey band on  
 559 left represents harzburgite not yet transformed into dunite. The results of the model for the lowermost  
 560 cell correspond to those of the single-cell melt percolation model shown in Fig. 6. Due to the strong  
 561 buffering effect of the Os-rich peridotite, the Os isotope compositions of the peridotite cells will be  
 562 successively less affected by melt interaction during the progressive ascent of the melt through the  
 563 channel. The compositions of the uppermost cell are hardly modified at all.

564

#### 5.4. *Concordance of model with geological observations*

565

The radiogenic Os composition of the MTZ dunites and overlying lower crust implies that they cannot

566

have been fed by melts percolating through and equilibrating with a network of coalescing dunite

567

channels. This inference is consistent with the scarcity of several meter thick dunites throughout the

568

MMS. These observations contrast with the common view that large tabular dunites are frequent

569

throughout the mantle section, as first expressed in the schematic diagram of Lippard et al. (1986). In

570

the southern massifs of the Oman ophiolite, dunites are abundant in only three areas: (1) the MTZ,

571

which structural, petrographic and geochemical evidence (Boudier and Nicolas, 1995; Godard et al.,

572

2000; Koga et al., 2001; Rospabé et al., 2018) suggest formed *in situ*, while the overlying crust was still

573

partially molten; (2) the BBU above the metamorphic sole; (3) the vicinity of the spectacular, yet

574

atypical, giant Batin dunite body. In contrast, dunites are very rare even in the cores of mantle diapirs,

575

thought to represent magmatic feeder zones for the overlying crust. The model of porous melt

576

transport in vertical dunite channels (Kelemen et al., 1995) would predict the existence of large

577

vertical dunite roots beneath the thick MTZ in these areas. Yet, such dunite conduits have not been

578

found within any of the mantle diapirs. Alternatively, it has been proposed that upwardly migrating

579

melts pool along a permeability barrier (e.g. the top of the melting region, the base of the lithosphere

580

or the locus of plagioclase crystallization) and then migrate laterally, "uphill", along this boundary

581

towards the ridge axis through porous flow channels or as "porosity waves" (Hebert and Montési,

582

2010; Sparks and Parmentier, 1991). At first glance, the basal dunite bands could correspond to the

583

geometry suggested by this model. However, their Os isotope compositions are equivalent to those of

584

the surrounding harzburgite, indicating they did not serve as pathways for the much more radiogenic

585

melts that reached the MTZ and the lower crust.

586

If, as the geochemical and structural data indicate, melt did not migrate to the Moho through dunite

587

channels, either vertically or along a putative permeability barrier, how was it transported? It appears

588

to have traveled rapidly across the mantle section, possibly leaving very little chemical and isotopic

589

imprint, except perhaps as small dunite reaction zones similar to those developed at the margins of

590

the later cross-cutting veins (Fig. 2b, 7a). If such dunites formed while the mantle was still flowing

591 under asthenospheric conditions, they could have been transposed and stretched. These dunites may  
592 be difficult to identify now, or may correspond to the rare thin concordant bands observed in the  
593 MMS (insert in [Fig. 2b](#) and [Table A.1](#)). The modeling of [Stevenson \(1989\)](#) and the experimental results  
594 of [Daines and Kohlstedt \(1994\)](#) predict the formation of veins in the melting mantle. Rapid melt  
595 transport through hydrofractures in the asthenosphere is a physically complex process ([Richardson,](#)  
596 [1998](#); [Rubin, 1995](#)), whose viability remains to be better established, but this process would fit our  
597 structural and geochemical data.

598 **6. Conclusions**

599 Dunite is distributed in the mantle section of the southeastern Oman ophiolite in three distinct  
600 domains: (1) the Moho Transition Zone, a horizontal dunitic melt storage and reaction zone at the  
601 summit of the mantle section, representing by far the largest volume of dunite; (2) the harzburgitic  
602 main mantle section, just below the MTZ, crosscut by sporadic dikes rimmed by dunitic reaction zones  
603 and rarer concordant bands; and (3) the basal banded unit, with many concordant dunitic bands  
604 above the metamorphic sole.

605 Though these three types of dunite cannot be distinguished petrographically, their Os isotope  
606 compositions are strongly correlated with their structural context. Basal dunitites, like harzburgites  
607 throughout the massifs, have  $^{187}\text{Os}/^{188}\text{Os}_{95\text{Ma}}$  ratios in the range of abyssal peridotites, while the  
608 dunitic veins and bands of the MMS have variable but somewhat more radiogenic compositions.  
609 Critically, MTZ dunitites have highly radiogenic Os isotope compositions, similar to those of the  
610 overlying lower crust. Such compositions are inconsistent with models that call on melt transport to  
611 the ridge by porous flow through dunite channels, as the high  $^{187}\text{Os}/^{188}\text{Os}$  ratios of the Os-poor melts  
612 would be erased by equilibration with the unradiogenic compositions of the Os-rich dunitites through  
613 which they travel. Furthermore, the absence of thick vertical dunite bodies in mantle diapirs, thought  
614 to represent magmatic feeder zones for the overlying crust, also argues that dunite channels are not  
615 the dominant pathway of melt transport to the ridge. Thus, our results reveal the need for a process,  
616 possibly hydrofracturing, that can rapidly bring radiogenic melts from the source region to the Moho  
617 without significant equilibration with dunite or harzburgite of the surrounding mantle.

618 **Acknowledgements**

619 We are very grateful to C. Zimmermann for her helpful assistance during Re-Os chemistry and isotope  
620 analyses by N-TIMS and MC-ICP-MS. We also thank C. Parmentier for her help with chemistry, D.  
621 Cividini and A. Schumacher for their technical support during MC-ICP-MS sessions, the SARM staff for  
622 whole-rock major element analyses, C. Martin (Géosciences Montpellier) and L. Causse (AETE-ISO  
623 platform, OSU-OREME/Université de Montpellier) for their assistance during whole-rock trace element  
624 chemical preparation and analysis by quadrupole ICP-MS, C. Prigent for providing her samples from  
625 the Haylayn massif and E. Grellier for her petrographic observations during her Master. Informal  
626 discussions and contributions during fieldwork from F. Boudier, S. Singh and D. Levy were also highly  
627 appreciated. We thank B. O'Driscoll and H. Becker for their thorough and constructive reviews.  
628 Financial support was provided by the TelluS Program of CNRS/INSU. We are finally highly grateful to  
629 the Ministry of Commerce and Industry, Sultanate of Oman, for its hospitality and its permission to  
630 undertake field sampling in Oman.

631 **Author Contributions**

632 D. Klaessens, D. Jouselin and L. Reisberg participated in fieldwork. D. Jouselin provided geological  
633 context. C. Aupart completed initial analyses. D. Klaessens completed most of the analyses and wrote  
634 the initial manuscript. L. Reisberg supervised Re-Os analyses and modeling. M. Godard oversaw trace  
635 element analyses. D. Klaessens, L. Reisberg and D. Jouselin discussed the results and their  
636 implications. All authors assisted in the final revisions to the manuscript.

637 ***CRediT author statement***

638 Delphine Klaessens: Conceptualization, Methodology, Formal analysis, Validation, Investigation,  
639 Visualization, Writing - Original Draft, Writing - Review & Editing

640 Laurie Reisberg: Conceptualization, Methodology, Investigation, Writing - Review & Editing,  
641 Supervision, Funding acquisition

642 David Joussein: Conceptualization, Investigation, Writing - Review & Editing, Supervision, Funding  
643 acquisition

644 Marguerite Godard: Validation, Writing - Review & Editing, Supervision

645 Claire Aupart: Formal analysis, Investigation, Writing - Review & Editing

646 **Competing Interests statement**

647 None of the authors have competing interests.

648 **References**

- 649 1. Ahern, J.L., Turcotte, D.L., 1979. Magma migration beneath an ocean ridge. *Earth Planet. Sci. Lett.*  
650 45, 115–122. [https://doi.org/10.1016/0012-821X\(79\)90113-4](https://doi.org/10.1016/0012-821X(79)90113-4)
- 651 2. Ahmed, A.H., Hanghøj, K., Kelemen, P.B., Hart, S.R., Arai, S., 2006. Osmium isotope systematics of  
652 the Proterozoic and Phanerozoic ophiolitic chromitites: In situ ion probe analysis of primary Os-  
653 rich PGM. *Earth Planet. Sci. Lett.* 245, 777–791. <https://doi.org/10.1016/j.epsl.2006.03.021>
- 654 3. Alabaster, T., Pearce, J.A., Malpas, J., 1982. The volcanic stratigraphy and petrogenesis of the  
655 Oman ophiolite complex. *Contrib. to Mineral. Petrol.* 81, 168–183.  
656 <https://doi.org/10.1007/BF00371294>
- 657 4. Bartholomew, I.D., 1983. The primary structures and fabrics of the upper mantle and lower crust  
658 from ophiolite complexes. The Open University, Milton Keynes.
- 659 5. Becker, H., Carlson, R.W., Shirey, S.B., 2004. Slab-derived osmium and isotopic disequilibrium in  
660 garnet pyroxenites from a Paleozoic convergent plate margin (lower Austria). *Chem. Geol.* 208,  
661 141–156. <https://doi.org/10.1016/j.chemgeo.2004.04.009>
- 662 6. Becker, H., Dale, C.W., 2016. Re–Pt–Os isotopic and highly siderophile element behavior in oceanic  
663 and continental mantle tectonites. *Rev. Mineral. Geochemistry* 81, 369–440.  
664 <https://doi.org/10.2138/rmg.2016.81.7>
- 665 7. Becker, H., Shirey, S.B., Carlson, R.W., 2001. Effects of melt percolation on the Re–Os systematics  
666 of periodites from a Paleozoic convergent plate margin. *Earth Planet. Sci. Lett.* 188, 107–121.

- 667 [https://doi.org/10.1016/S0012-821X\(01\)00308-9](https://doi.org/10.1016/S0012-821X(01)00308-9)
- 668 8. Bezar, R., Turner, S., Schaefer, B., Yogodzinski, G., Hoernle, K., 2021. Os isotopic composition of  
669 western Aleutian adakites: Implications for the Re/Os of oceanic crust processed through hot  
670 subduction zones. *Geochim. Cosmochim. Acta* 292, 452–467.  
671 <https://doi.org/10.1016/j.gca.2020.10.009>
- 672 9. Boudier, F., Coleman, R.G., 1981. Cross section through the peridotite in the Samail Ophiolite,  
673 southeastern Oman Mountains. *J. Geophys. Res. Solid Earth* 86, 2573–2592.  
674 <https://doi.org/10.1029/JB086iB04p02573>
- 675 10. Boudier, F., Nicolas, A., 1995. Nature of the Moho Transition zone in the Oman ophiolite. *J. Petrol.*  
676 36, 777–796. <https://doi.org/10.1093/petrology/36.3.777>
- 677 11. Boudier, F., Nicolas, A., 1977. Structural control on the partial melting of the Lanzo peridotite, in:  
678 AGU Chapman Conf. Proc. Bull. 96. Geol. Min. Industries, Oregon Dep.
- 679 12. Boudier, F., Nicolas, A., Ildefonse, B., Jousset, D., 1997. EPR microplates, a model for the Oman  
680 Ophiolite. *Terra Nov.* 9, 79–82. <https://doi.org/10.1111/j.1365-3121.1997.tb00007.x>
- 681 13. Braun, M.G., Kelemen, P.B., 2002. Dunite distribution in the Oman Ophiolite: Implications for melt  
682 flux through porous dunite conduits. *Geochemistry, Geophys. Geosystems* 3, 1–21.  
683 <https://doi.org/10.1029/2001GC000289>
- 684 14. Brenan, J.M., Bennett, N.R., Zajacz, Z., 2016. Experimental results on fractionation of the highly  
685 siderophile elements (HSE) at variable pressures and temperatures during planetary and magmatic  
686 differentiation. *Rev. Mineral. Geochemistry* 81, 1–87. <https://doi.org/10.2138/rmg.2016.81.1>
- 687 15. Büchl, A., Brüggemann, G.E., Batanova, V.G., Hofmann, A.W., 2004. Os mobilization during melt  
688 percolation: The evolution of Os isotope heterogeneities in the mantle sequence of the Troodos  
689 ophiolite, Cyprus. *Geochim. Cosmochim. Acta* 68, 3397–3408.  
690 <https://doi.org/10.1016/j.gca.2004.02.005>
- 691 16. Büchl, A., Brüggemann, G.E., Batanova, V.G., Münker, C., Hofmann, A.W., 2002. Melt percolation  
692 monitored by Os isotopes and HSE abundances: A case study from the mantle section of the  
693 Troodos Ophiolite. *Earth Planet. Sci. Lett.* 204, 385–402. <https://doi.org/10.1016/S0012->

694 821X(02)00977-9

695 17. Daines, M.J., Kohlstedt, D.L., 1994. The transition from porous to channelized flow due to  
696 melt/rock reaction during melt migration. *Geophys. Res. Lett.* 21, 145–148.

697 <https://doi.org/10.1029/93GL03052>

698 18. Elkins, L.J., Bourdon, B., Lambart, S., 2019. Testing pyroxenite versus peridotite sources for marine  
699 basalts using U-series isotopes. *Lithos* 332–333, 226–244.

700 <https://doi.org/10.1016/j.lithos.2019.02.011>

701 19. Ernewein, M., Pflumio, C., Whitechurch, H., 1988. The death of an accretion zone as evidenced by  
702 the magmatic history of the Sumail ophiolite (Oman). *Tectonophysics* 151, 247–274.

703 20. Fonseca, R.O.C., Laurenz, V., Mallmann, G., Luguët, A., Hoehne, N., Jochum, K.P., 2012. New  
704 constraints on the genesis and long-term stability of Os-rich alloys in the Earth's mantle. *Geochim.*  
705 *Cosmochim. Acta* 87, 227–242. <https://doi.org/10.1016/j.gca.2012.04.002>

706 21. Gannoun, A., Burton, K.W., Day, J.M.D., Harvey, J., Schiano, P., Parkinson, I., 2016. Highly  
707 siderophile element and Os isotope systematics of volcanic rocks at divergent and convergent  
708 plate boundaries and in intraplate settings. *Rev. Mineral. Geochemistry* 81, 651–724.

709 <https://doi.org/10.2138/rmg.2016.81.11>

710 22. Godard, M., Bosch, D., Einaudi, F., 2006. A MORB source for low-Ti magmatism in the Semail  
711 ophiolite. *Chem. Geol.* 234, 58–78. <https://doi.org/10.1016/j.chemgeo.2006.04.005>

712 23. Godard, M., Jousset, D., Bodinier, J.L., 2000. Relationships between geochemistry and structure  
713 beneath a palaeo-spreading centre: A study of the mantle section in the Oman ophiolite. *Earth*  
714 *Planet. Sci. Lett.* 180, 133–148. [https://doi.org/10.1016/S0012-821X\(00\)00149-7](https://doi.org/10.1016/S0012-821X(00)00149-7)

715 24. Guilmette, C., Smit, M.A., van Hinsbergen, D.J.J., Gürer, D., Corfu, F., Charette, B., Maffione, M.,  
716 Rabeau, O., Savard, D., 2018. Forced subduction initiation recorded in the sole and crust of the  
717 Semail ophiolite of Oman. *Nat. Geosci.* 11, 688–695. <https://doi.org/10.1038/s41561-018-0209-2>

718 25. Hanghøj, K., Kelemen, P.B., Hassler, D., Godard, M., 2010. Composition and genesis of depleted  
719 mantle peridotites from the Wadi Tayin massif, Oman ophiolite; Major and trace element  
720 geochemistry, and Os isotope and PGE systematics. *J. Petrol.* 51, 201–227.

- 721 <https://doi.org/10.1093/petrology/egp077>
- 722 26. Hebert, L.B., Montési, L.G.J., 2010. Generation of permeability barriers during melt extraction at  
723 mid-ocean ridges. *Geochem. Geophys. Geosyst.* 11, Q12008.  
724 <https://doi.org/10.1029/2010GC003270>
- 725 27. Jébrak, M., 1997. Hydrothermal breccias in vein-type ore deposits: A review of mechanisms,  
726 morphology and size distribution. *Ore Geol. Rev.* 12, 111–134.
- 727 28. Jousselin, D., Nicolas, A., Boudier, F., 1998. Detailed mapping of a mantle diapir below a paleo-  
728 spreading center in the Oman ophiolite. *J. Geophys. Res. Solid Earth* 103, 18153–18170.  
729 <https://doi.org/10.1029/98JB01493>
- 730 29. Kelemen, P.B., 1990. Reaction between ultramafic rock and fractionating basaltic magma I. Phase  
731 relations, the origin of calc-alkaline magma series, and the formation of discordant dunite. *J.*  
732 *Petrol.* 31, 51–98. <https://doi.org/10.1093/petrology/31.1.51>
- 733 30. Kelemen, P.B., Shimizu, N., Salters, V.J.M., 1995. Extraction of mid-ocean-ridge basalt from the  
734 upwelling mantle by focused flow of melt in dunite channels. *Nature* 375, 747–753.  
735 <https://doi.org/10.1038/375747a0>
- 736 31. Koga, K.T., Kelemen, P.B., Shimizu, N., 2001. Petrogenesis of the crust-mantle transition zone and  
737 the origin of lower crustal wehrlite in the Oman ophiolite. *Geochemistry, Geophys. Geosystems* 2.  
738 <https://doi.org/10.1029/2000GC000132>
- 739 32. Kogiso, T., Hirschmann, M.M., Reiners, P.W., 2004. Length scales of mantle heterogeneities and  
740 their relationship to ocean island basalt geochemistry. *Geochim. Cosmochim. Acta* 68, 345–360.  
741 [https://doi.org/10.1016/S0016-7037\(03\)00419-8](https://doi.org/10.1016/S0016-7037(03)00419-8)
- 742 33. Lambart, S., Laporte, D., Schiano, P., 2009. An experimental study of focused magma transport and  
743 basalt-peridotite interactions beneath mid-ocean ridges: Implications for the generation of  
744 primitive MORB compositions. *Contrib. to Mineral. Petrol.* 157, 429–451.  
745 <https://doi.org/10.1007/s00410-008-0344-7>
- 746 34. Levasseur, S., Birck, J.L., Allègre, C.J., 1998. Direct measurement of femtomoles of osmium and the  
747  $^{187}\text{Os}/^{186}\text{Os}$  ratio in seawater. *Science* 282, 272–274.

- 748 <https://doi.org/10.1126/science.282.5387.272>
- 749 35. Lippard, S.J., Shelton, A.W., Gass, I.G., 1986. The Ophiolite of Northern Oman, in: The Geological  
750 Society Memoirs. Backwell Scientific Publications, London, p. 178.  
751 <https://doi.org/10.1144/GSL.MEM.1986.011.01.03>
- 752 36. Lorand, J.P., Alard, O., Godard, M., 2009. Platinum-group element signature of the primitive  
753 mantle rejuvenated by melt-rock reactions: evidence from Sumail peridotites (Oman Ophiolite).  
754 *Terra Nov.* 21, 35–40. <https://doi.org/10.1111/j.1365-3121.2008.00850.x>
- 755 37. Lorand, J.P., Luguet, A., 2016. Chalcophile and siderophile elements in mantle rocks: trace  
756 elements controlled by trace minerals. *Rev. Mineral. Geochemistry* 81, 441–488.  
757 <https://doi.org/10.2138/rmg.2016.81.08>
- 758 38. MacLeod, C.J., Lissenberg, C.J., Bibby, L.E., 2013. “Moist MORB” axial magmatism in the Oman  
759 ophiolite: The evidence against a mid-ocean ridge origin. *Geology* 41, 459–462.  
760 <https://doi.org/10.1130/G33904.1>
- 761 39. McCulloch, M.T., Gregory, R.T., Wasserburg, G.J., Taylor, H.P.J., 1981. Sm-Nd, Rb-Sr, and 18O/16O  
762 isotopic systematics in an oceanic crustal section: Evidence from the Samail Ophiolite. *J. Geophys.*  
763 *Res. Solid Earth* 86, 2721–2735. <https://doi.org/10.1029/JB086iB04p02721>
- 764 40. Meisel, T., Walker, R.J., Irving, A.J., Lorand, J.P., 2001. Osmium isotopic compositions of mantle  
765 xenoliths : A global perspective. *Geochim Cosmochim Acta* 65, 1311–1323.
- 766 41. Morgan, Z., Liang, Y., 2003. An experimental and numerical study of the kinetics of harzburgite  
767 reactive dissolution with applications to dunite dike formation. *Earth Planet. Sci. Lett.* 214, 59–74.  
768 [https://doi.org/10.1016/S0012-821X\(03\)00375-3](https://doi.org/10.1016/S0012-821X(03)00375-3)
- 769 42. Mungall, J.E., Brenan, J.M., 2014. Partitioning of platinum-group elements and Au between sulfide  
770 liquid and basalt and the origins of mantle-crust fractionation of the chalcophile elements.  
771 *Geochim. Cosmochim. Acta* 125, 265–289. <https://doi.org/10.1016/j.gca.2013.10.002>
- 772 43. Nicolas, A., 1986. A Melt Extraction Model Based on Structural Studies in Mantle Peridotites. *J.*  
773 *Petrol.* 27, 999–1022. <https://doi.org/10.1093/petrology/27.4.999>
- 774 44. Nicolas, A., Boudier, F., 2001. Oman & UAE ophiolite. *Mar. Geophys. Res.* 21.

- 775 45. Nicolas, A., Boudier, F., Ildefonse, B., Ball, E., 2000a. Accretion of Oman and United Arab Emirates  
776 ophiolite – Discussion of a new structural map. *Mar. Geophys. Res.* 21, 147–180.  
777 <https://doi.org/10.1023/A:1026769727917>
- 778 46. Nicolas, A., Ildefonse, B., Boudier, F., Lenoir, X., Ben Ismail, W., 2000b. Dike distribution in the  
779 Oman-United Arab Emirates ophiolite. *Mar. Geophys. Res.* 21, 269–287.  
780 <https://doi.org/10.1023/A:1026718026951>
- 781 47. Nicolas, A., Prinzhofer, A., 1983. Cumulative or Residual Origin for the Transition Zone in  
782 Ophiolites: Structural Evidence. *J. Petrol.* 24, 188–206. <https://doi.org/10.1093/petrology/24.2.188>
- 783 48. O’Driscoll, B., Day, J.M.D., Walker, R.J., Daly, J.S., McDonough, W.F., Piccoli, P.M., 2012. Chemical  
784 heterogeneity in the upper mantle recorded by peridotites and chromitites from the Shetland  
785 Ophiolite Complex, Scotland. *Earth Planet. Sci. Lett.* 333–334, 226–237.  
786 <https://doi.org/10.1016/j.epsl.2012.03.035>
- 787 49. O’Driscoll, B., González-Jiménez, J.M., 2016. Petrogenesis of the Platinum-Group Minerals. *Rev.*  
788 *Mineral. Geochemistry* 81, 489–578. <https://doi.org/10.2138/rmg.2016.81.09>
- 789 50. O’Hara, M.J., 1965. Primary magmas and the origin of basalts. *Scottish J. Geol.* 1, 19–40.  
790 <https://doi.org/10.1144/sjg01010019>
- 791 51. Peucker-Ehrenbrink, B., Hanghøj, K., Atwood, T., Kelemen, P.B., 2012. Rhenium-osmium isotope  
792 systematics and platinum group element concentrations in oceanic crust. *Geology* 40, 199–202.  
793 <https://doi.org/10.1130/G32431.1>
- 794 52. Ravizza, G., Blusztajn, J., Prichard, H.M., 2001. Re-Os systematics and platinum-group element  
795 distribution in metalliferous sediments from the Troodos ophiolite. *Earth Planet. Sci. Lett.* 188,  
796 369–381. [https://doi.org/10.1016/S0012-821X\(01\)00337-5](https://doi.org/10.1016/S0012-821X(01)00337-5)
- 797 53. Richardson, C.N., 1998. Melt flow in a variable viscosity matrix. *Geophys. Res. Lett.* 25, 1099–1102.  
798 <https://doi.org/10.1029/98GL50565>
- 799 54. Rioux, M., Bowring, S., Kelemen, P.B., Gordon, S., Dudás, F., Miller, R., 2012. Rapid crustal  
800 accretion and magma assimilation in the Oman-U.A.E. ophiolite: High precision U-Pb zircon  
801 geochronology of the gabbroic crust. *J. Geophys. Res. Solid Earth* 117, 1–12.

- 802 <https://doi.org/10.1029/2012JB009273>
- 803 55. Rospabé, M., Benoit, M., Ceuleneer, G., Hodel, F., Kaczmarek, M.A., 2018. Extreme geochemical  
804 variability through the dunitic transition zone of the Oman ophiolite : Implications for melt/fluid-  
805 rock reactions at Moho level beneath oceanic spreading centers. *Geochim Cosmochim Acta* 234,  
806 1–23. <https://doi.org/10.1016/j.gca.2018.05.012>
- 807 56. Rubin, A.M., 1995. Propagation of Magma-Filled Cracks. *Annu. Rev. Earth Planet. Sci.* 23, 287–336.  
808 <https://doi.org/10.1146/annurev.ea.23.050195.001443>
- 809 57. Senda, R., Suzuki, K., Morishita, T., Takazawa, E., The Oman Drilling Project Science Party, 2020.  
810 The PGE and Os isotope variations in the mantle transition zone from the Samail Ophiolite from  
811 the Cores of the Oman Drilling Project, in: *International Conference on Ophiolites and the Oceanic  
812 Lithosphere: Results of the Oman Drilling Project and Related Research*. Sultan Qaboos University,  
813 Muscat, Sultanate of Oman, p. 1.
- 814 58. Sergeev, D.S., Dijkstra, A.H., Meisel, T., Brüggmann, G.E., Sergeev, S.A., 2014. Traces of ancient  
815 mafic layers in the Tethys oceanic mantle. *Earth Planet. Sci. Lett.* 389, 155–166.  
816 <https://doi.org/10.1016/j.epsl.2013.10.039>
- 817 59. Smoliar, M.I., Walker, R.J., Morgan, J.W., 1996. Re-Os Ages of Group IIA, IIIA, IVA, and IVB Iron  
818 Meteorites. *Science* 271, 1099 LP – 1102. <https://doi.org/10.1126/science.271.5252.1099>
- 819 60. Sparks, D.W., Parmentier, E.M., 1991. Melt extraction from the mantle beneath spreading centers.  
820 *Earth Planet. Sci. Lett.* 105, 368–377. [https://doi.org/10.1016/0012-821X\(91\)90178-K](https://doi.org/10.1016/0012-821X(91)90178-K)
- 821 61. Stevenson, D.J., 1989. Spontaneous small-scale melt segregation in partial melts undergoing  
822 deformation. *Geophys. Res. Lett.* 16, 1067–1070. <https://doi.org/10.1029/GL016i009p01067>
- 823 62. Stolper, E., 1980. A phase diagram for mid-ocean ridge basalts: Preliminary results and implications  
824 for petrogenesis. *Contrib. to Mineral. Petrol.* 74, 13–27. <https://doi.org/10.1007/BF00375485>
- 825 63. Vernières, J., Godard, M., Bodinier, J.L., 1997. A plate model for the simulation of trace element  
826 fractionation during partial melting and magma transport in the Earth’s upper mantle. *J. Geophys.  
827 Res. B Solid Earth* 102, 24771–24784. <https://doi.org/10.1029/97jb01946>
- 828 64. Xiong, Q., Xu, Y., González-Jiménez, J.M., Liu, J., Alard, O., Zheng, J.P., Griffin, W.L., O’Reilly, S.Y.,

829 2020a. Sulfide in dunite channels reflects long-distance reactive migration of mid-ocean-ridge  
830 melts from mantle source to crust: A Re-Os isotopic perspective. *Earth Planet. Sci. Lett.* 531, 1–10.  
831 <https://doi.org/10.1016/j.epsl.2019.115969>

832 65. Xiong, Q., Xu, Y., González-Jiménez, J.M., Liu, J., Alard, O., Zheng, J.P., Griffin, W.L., O'Reilly, S.Y.,  
833 2020b. Corrigendum to “Sulfide in dunite channels reflects long-distance reactive migration of  
834 mid-ocean-ridge melts from mantle source to crust: A Re-Os isotopic perspective.” *Earth Planet.*  
835 *Sci. Lett.* 535, 1. <https://doi.org/10.1016/j.epsl.2020.116136>